Effective Radius of Cloud Droplets by Ground-Based Remote Sensing: Relationship to Aerosol

Byung-Gon Kim[1,2], Stephen E. Schwartz[1,*],
Mark A. Miller[1], Qilong Min[3]

Submitted to JGR, April-25-2003
Revised July 31, 2003
Accepted August 22, 2003

Running Title:
Effective Radius of Cloud Droplets

*Corresponding author: Environmental Sciences Department, Brookhaven National Laboratory, 75 Rutherford Drive, Upton, NY 11973 USA, email ses@bnl.gov
[1]Environmental Sciences Department, Brookhaven National Laboratory, Upton, NY 11973 USA
[2]Now at Atmospheric & Oceanic Sciences Program, Princeton University, Princeton, NJ 08542 USA
[3]Atmospheric Science Research Center, State University of New York at Albany, 251 Fuller Road, Albany, NY, 12203 USA

Abstract

Enhancement of cloud droplet number concentration by anthropogenic aerosols has previously been demonstrated by in-situ measurements, but there remains large uncertainty in the resultant enhancement of cloud optical depth and reflectivity. Detection of this effect is made difficult by the large inherent variability in cloud liquid water path (LWP); the dominant influence of LWP on optical depth and albedo masks any aerosol influences. Here we use ground-based remote sensing of cloud optical depth (τ_c) by narrowband radiometry and LWP by microwave radiometry to determine the dependence of optical depth on LWP, thereby permitting examination of aerosol influence; the method is limited to complete overcast conditions with single layer clouds, as determined mainly by millimeter wave cloud radar. Measurements in north central Oklahoma on 13 different days in the year 2000 show wide variation in LWP and optical depth on any given day, but with near linear proportionality between the two quantities; variance in LWP accounts as much as 97% of the variance in optical depth on individual days and for about 63 % of the variance in optical depth for the whole data set. The slope of optical depth vs. LWP is inversely proportional to the effective radius of cloud droplets (r_e); event-average cloud droplet effective radius ranged from 5.6 ± 0.1 to 12.3 ± 0.6 μm (average ± uncertainty in the mean). This effective radius is negatively correlated with aerosol light scattering coefficient at the surface as expected for the aerosol indirect effect; the weak correlation (R^2 = 0.24) might be due in part to vertically decoupled structure of aerosol particle concentration and possible meteorological influence such as vertical wind shear. Cloud albedo and radiative forcing for a given LWP are highly sensitive to effective radius; for solar zenith angle 60° and typical LWP of 100 g m^{-2}, as effective radius decreases from 10.2 to 5.8 μm determined on different days, the resultant decrease in calculated net shortwave irradiance at the top of the atmosphere (Twomey forcing) is about 50 W m^{-2}.

1. Introduction

Aerosols affect global climate directly by scattering or absorbing radiation, and indirectly by altering cloud microphysical and radiative properties. Direct aerosol forcing has been estimated to be globally of similar magnitude and opposite sign to greenhouse gas forcing [Charlson et al., 1992; Kiehl and Briegleb, 1993; IPCC, 2001]. While such global estimates are useful for planetary radiation balance calculations, direct aerosol radiative forcing acts primarily on local to regional scales because of the nonuniform distribution of aerosol particles in the atmosphere. Increases in anthropogenic sources of cloud condensation nuclei (CCN) can increase cloud albedo by increasing the concentration and reducing the size of cloud droplets [Twomey, 1977], usually referred to as the first indirect effect of aerosol on climate. Albrecht [1989] suggested that the increased number concentration of smaller droplets suppresses precipitation and results in the increase of cloud lifetime and the average cloud cover on earth. Additionally, reduction in cloud cover caused by absorption of solar radiation in haze layers [Hansen et al., 1997; Ackerman et al., 2000] may be considered a 'semidirect effect'. Recently Liu and Daum [2002] showed that dispersion forcing derived from changes of the size distribution of cloud droplets in air influenced by anthropogenic emissions acts to diminish the cooling effect. The magnitudes of the various kinds of indirect radiative forcing are quite uncertain, because they involve subtle changes in cloud radiative properties and lifetimes [Schwartz and Slingo, 1996, Penner et al., 2001 in IPCC; Ramaswamy et al., 2001 in IPCC].

Studies relating the enhancement of cloud droplet concentrations to the increase of cloud albedo have typically been limited to in-situ and remotely sensed characterization of cloud microphysics during intensive field campaigns, such as the First International Satellite Cloud Climatology Project (ISCCP) Regional Experiment (FIRE) ship track study [Radke et al., 1989], the comparison of pristine maritime air and continental air influenced by industrial emissions during the Atlantic Stratocumulus Transition Experiment [ASTEX; Albrecht et al., 1995] and the 2nd Aerosol Characterization Experiment [ACE-2; Brenguier et al., 2000].

Large-scale satellite surveys have shown cloud droplet effective radius of warm clouds to be systematically lower [Han et al., 1994; Han et al., 1998] and number concentration systematically greater [Han et al., 1998] in the anthropogenically influenced Northern

Hemisphere than in the relatively unperturbed Southern Hemisphere, consistent with the Twomey mechanism of indirect aerosol forcing. Likewise, fairly strong spatial correlations have been reported of monthly mean aerosol optical depth and number concentration with effective radius (negative correlation) and optical depth (positive correlation) of low clouds [Wetzel and Stowe, 1999; Nakajima et al., 2001]. Breon et al. [2001] also observed smaller cloud droplets over highly polluted continental areas and downwind of continents from satellite measurements. Recently, influences of anthropogenic aerosols on cloud were demonstrated in several-day episodes when enhanced aerosol loading was indicated by a chemical transport model, using satellite measurements of optical depth and effective radius [Harshvardhan et al., 2002; Schwartz et al., 2002].

Ground-based remote sensing has the advantage of continuous operation over long periods and can examine long-term trends in aerosol properties [Michalsky et al., 2001; Sheridan et al., 2001]. Above all, an integrated data set is available for detailed analyses. The U.S. Department of Energy's Atmospheric Radiation Measurement (ARM) program established the Southern Great Plains (SGP, north-central Oklahoma) Cloud and Radiation Testbed site to conduct multiple continuous in-situ and remote measurements of radiation and cloud and aerosol properties over extended periods [Stokes and Schwartz, 1994]. This program has begun to lay the foundation for improvement of climate models and serves as an important testbed for the physics of climate and weather-prediction models [Ackerman and Stokes, 2003].

Here we use ground-based remote sensing of cloud optical depth (τ_c) by narrow-band visible-wavelength radiometry and LWP by microwave radiometry to determine the dependence of optical depth on LWP. The goal of this study is to examine the characteristics of cloud droplet effective radius (r_e) and its relationship to aerosol concentration and meteorological conditions using data from the SGP ARM archive for the year 2000. Cloud radar, ceilometer, and lidar together are used to determine the cloud boundaries. Fully overcast cloudy situations are more carefully screened by shortwave radiometry. Aerosol scattering coefficients are retrieved from in-situ measurements at the surface and intermittently by aircraft flights. Vertical profiles of wind and temperature are obtained from intermittent balloon soundings.

2. Data and Method

The data for this study were obtained principally from the ARM archive, which stores and distributes data collected from these experiments through the public access interface (http://www.archive.arm.gov). The primary instruments used in this study at the SGP site (97.48°W, 36.61°N) in Oklahoma are summarized in Table 1.

The most favorable cloud type for testing relations between radiation and microphysical properties is a widespread low-level non-precipitating, liquid water cloud layer without interference from higher-level ice clouds. Suitable conditions were carefully selected by examination of time series of retrieved cloud layers for the year 2000. Completely overcast sky is necessary for the determination of cloud optical depth using a MultiFilter Rotating Shadowband Radiometer (MFRSR). Spatial uniformity is required on account of the near hemispheric field-of-view, cosine-response detector of MFRSR (120°; full width at half maximum).

Cloud boundaries were retrieved from Active Remotely-Sensed Cloud Locations (ARSCL) value-added product (VAP), which combines data from active remote sensors, mainly Millimeter Wave Cloud Radar (MMCR), micro-pulse lidar, and ceilometer, to determine cloud boundaries [Clothiaux et al., 2000].

Situations potentially suitable for the study were further screened using shaded and unshaded irradiances measured by pyranometers. A suite of pyranometers measures downwelling total hemispheric irradiance, downwelling diffuse irradiance, and upwelling diffuse irradiance. An unshaded pyranometer provides measurements of total direct and diffuse irradiance components; a second pyranometer mounted on an automatic solar tracker, equipped with a shade mechanism to block the direct solar rays, provides measurements of diffuse irradiance. Lastly, the presence of complete overcast sky is confirmed by the estimation of clear-sky shortwave irradiance and fractional sky cover by a method that uses hemispheric broadband total and diffuse shortwave irradiance measurements to identify clear-sky periods using the known characteristics of typical clear-sky irradiance time scales, and applies an empirical fitting algorithm that uses a minimum absolute deviation technique to estimate both the clear-sky total shortwave irradiance and the ratio of diffuse to total shortwave irradiance as a function of solar zenith angle [cloud fraction VAP; Long and Ackerman, 2000].

The MFRSR takes spectral measurements of direct normal, diffuse horizontal, and total horizontal solar irradiances [Harrison et al., 1994] at nominal wavelengths of 415, 500, 615, 673, 870, and 940 nm. The sampling interval is 20 seconds. Min and Harrison [1996b] have developed a family of inversion methods to infer optical properties of warm clouds from surface measurements of narrowband spectral irradiance. Cloud optical depth is obtained using the observed atmospheric transmittance (rather than absolute irradiance), and surface albedo [Min and Harrison, 1996b] for solar zenith angle (SZA, θ_0) less than 75°. The MFRSR allows accurate determination of both quantities without requiring absolute calibration because it measures both total horizontal irradiance and direct-normal irradiance using the same detectors by a blocking technique. Consequently Langley regression of the direct-normal irradiance taken on stable clear days can be used to extrapolate the instrument's response to the top of atmosphere, and this calibration can then be applied to the total horizontal irradiance on overcast periods. Transmittances are calculated subsequently under cloudy conditions as the ratio of the MFRSR signal to the extrapolated top-of-atmosphere value.

We use climatological atmospheric gas profiles for Rayleigh scattering, and select the wavelength bandpass at 415 nm to avoid all gaseous absorption, except for NO_2, which has negligible impact under normal conditions. Several other factors favor the 415 nm bandpass compared to those in the 500 to 800 nm range: when snow is absent (as was the case for all events reported here) terrestrial albedos at 415 nm are significantly lower than at longer wavelengths and relatively constant (0.036 at SGP site); the effective radius is also less sensitive to single scattering albedo and asymmetry parameter.

Figure 1a shows the dependence of atmospheric transmittance on cloud optical depth (τ_c) evaluated with a radiative transfer model SBDART [Santa Barbara DISORT Atmospheric Radiative Transfer; Ricchiazzi et al., 1998] that is based on the DISORT algorithm for discrete-ordinate-method radiative transfer in multiple scattering and emitting layered media [Stamnes et al., 1988]. Here atmospheric transmittance is evaluated as the ratio of downwelling irradiance at the surface to that at the top of the atmosphere for a narrow wavelength band corresponding to the 415 nm channel of the MFRSR. Surface albedo and other conditions are also comparable to the measurement conditions; the dependence of transmittance on τ_c is sensitive to solar zenith angle but relatively insensitive to other variables, notably cloud droplet effective radius r_e, as shown in the figure, and

column water vapor. The transmittance is sensitive to surface albedo at higher values of albedo such as 0.15 - 0.20 characteristic of bare or vegetated soils at longer wavelengths in the shortwave, but quite insensitive at low surface albedo characteristic of 415 nm. Measurement of transmittance readily allows inversion to cloud optical depth as shown in Figure 1b, which displays a nearly linear dependence of optical depth on the inverse of transmittance, again quite insensitive to the value of r_e employed in the retrieval. This insensitivity allows cloud optical depth to be retrieved without *a priori* knowledge of the effective radius.

As is standard, we parameterize the cloud droplet optics in terms of r_e and total liquid water path based on Mie theory [Slingo, 1989; Hu and Stamnes, 1993]. For the results presented here cloud optical depth is retrieved by a Nonlinear Least Squares Method (NLSM), implemented through the linearized iteration described by Bevington [1969], in conjunction with an adjoint formulation of radiative transfer to speed up the computation [Min and Harrison, 1996a]. The advantage of this approach over other retrieval algorithms based on broadband measurements or normalized difference cloud indices from ground-based systems [Leontyeva and Stamnes, 1996; Dong et al., 2002; Marshak et al., 2000] is that it minimizes uncertainties associated with absolute calibration of measurements, surface albedo variation across the shortwave, and the interference of various gaseous absorptions (particularly water vapor).

Time-series measurements of column-integrated amounts of water vapor and liquid water are provided from the Microwave Radiometer (MWR), a sensitive microwave receiver. Vertical liquid water path at SGP is measured every 20 seconds by a zenith-viewing Radiometrics WVR-1100 MWR operating at frequencies of 23.8 and 31.4 GHz [Liljegren, 2000]. Liquid water in the atmosphere emits in a continuum dominating the 31.4 GHz observation, whereas water vapor dominates the 23.8 GHz channel. The field of view is 5.9° at 23.8 GHz and 4.5° at 31.4 GHz. Other studies [Liljegren et al., 2001; Dong et al., 2002] have used somewhat different algorithms for retrieval of LWP from microwave radiometer measurements; these different algorithms yield values of LWP that differ typically by 10%, as discussed below.

Aerosol light scattering coefficient (σ_{sp}) is measured by integrating nephelometers at the surface and during intermittent aircraft flights [Sheridan et al., 2001]. At the surface, two nephelometers (TSI Model 3563) and a humidifier measure σ_{sp} as a function of relative

humidity (RH) at three visible wavelengths (nominally 450, 550, and 700 nm). The two nephelometers are connected in series separated by humidity control system [Anderson and Ogren, 1998]. Here we use measurements at low RH ≤ 40%, representative of the light scattering coefficient of the dry aerosol. Aerosol size for this study is restricted to particles of aerodynamic diameter less than 1 μm as determined by a virtual impactor. Measurements are available as 1-minute averages for five 6-minute intervals per hour. These data were downloaded from http://www.cmdl.noaa.gov/aero/data/. In-situ Aerosol Profiling (IAP) flights obtain a data set of vertical distributions of aerosol scattering and absorption coefficients above the surface site 2 to 3 times a week.

Atmospheric vertical structure is obtained by the Balloon-Borne Sounding System (BBSS), which provides vertical profiles of both the thermodynamic state of the atmosphere, and the wind speed and direction. Pressure, temperature, relative humidity, wind speed, and wind direction are obtained every 10 seconds during a free-balloon ascent. Balloons are usually launched 4 times a day but 8 times a day during Intensive Observation Periods. The Richardson number (Ri) is evaluated from the sonde measurements as the ratio of buoyancy divided by wind shear [Stull, 1997].

$$Ri = \frac{g}{\bar{\theta}_l} \frac{\frac{d\theta_i}{dz}}{\left(\frac{du_i}{dz}\right)^2} \tag{1}$$

Here θ_i is potential temperature at level i, u_i wind speed at level i, g gravitational acceleration, and $\bar{\theta}_l$ mean potential temperature within the layer.

3. Effective Radius of Cloud Droplets

Cloud droplet effective radius (r_e), a key property of clouds governing their radiative transfer [Hansen and Travis, 1974], is defined as the ratio of the third to second moments of the size distribution of the cloud drop number concentration. For a spatially homogeneous cloud,

$$r_e = \frac{\mu_3}{\mu_2} = \frac{\int N(r) r^3 dr}{\int N(r) r^2 dr} \tag{2}$$

where $N(r)$ is size distribution of the cloud drops and r is the cloud drop radius. This definition is readily extended to vertically inhomogeneous clouds, justifying the determination of r_e even for such non-homogeneous clouds.

$$r_e = \frac{\mu_3}{\mu_2} = \frac{\iint N(r,z) r^3 dr dz}{\iint N(r,z) r^2 dr dz} \tag{3}$$

The integrals are taken over drop radius and over the depth of the cloud. Accordingly, this definition allows r_e to be evaluated in terms of measured LWP (L) and τ_c;

$$L = \frac{4\pi}{3} \rho_w \int \int r^3 N(r,z) dr dz \tag{4}$$

$$\tau_c = \iint \pi r^2 Q_e(r) N(r,z) dr dz \tag{5}$$

where ρ_w is density of liquid water and $Q_e(r)$ is the extinction efficiency for a cloud droplet of radius r.

For cloud droplets of radius much greater than the wavelength of visible light $Q_e(r)$ may be approximated within a few percent as a constant, $Q_e \approx 2$ [Hansen and Travis, 1974; Twomey, 1977; van de Hulst, 1981]. Hence r_e can be estimated from τ_c and LWP [Han et al., 1994; Stephens, 1984]:

$$r_{e,r} = \frac{3}{2} \frac{L}{\rho_w \tau_c} \tag{6}$$

where the subscript r denotes that r_e is evaluated from the ratio L / τ_c.The effective radius determined in this way is the appropriate vertically integrated quantity governing radiative transfer of the cloud because both τ_c from MFRSR and LWP from MWR come from vertically integrated retrievals.

In view of the dependence of Mie scattering properties on cloud drop radius we retrieve effective radius by an iterative procedure (Min and Harrison, 1996 a, b) that takes these

dependences into account. Most important is the variation of extinction efficiency (affecting retrieval of r_e from τ_c and LWP). Values of effective radius retrieved in this way, $r_{e,M}$, (the subscript M denotes the Mie scattering retrieval) are compared to those obtained using Eq. (6) to ascertain the importance of this effect.

Cloud droplet effective radius has also been retrieved by other investigators using methods similar to those reported here [Dong et al., 1997; Dong et al., 1998; Li et al., 1999], the major difference being the determination of cloud optical depth by broadband shortwave radiometry rather than narrow band radiometry as employed here. Comparisons with those results are presented and discussed in section 4.

For the determination of cloud reflectivity, cloud-top spherical albedo (α_{sph}) is calculated for visible and near-visible radiation according to the asymptotic expression for conservative scattering of Harshvardhan and King [1993] as implemented by Schwartz et al. [2002]:

$$\alpha_{sph} \approx \frac{\tau_c(1-g)+0.097}{\tau_c(1-g)+1.43} \tag{7}$$

where g is the asymmetry parameter, which ranges from 0.834 to 0.872 as effective radius ranges from 6 μm to 19 μm.

4. Cloud Properties

There were 13 analysis days in the year 2000 which had suitable episodes of cloud cover that met the established selection criteria for continuous periods of two hours or more. Cloud properties and other relevant data are summarized in Table 2. Low-level and thin cloudy days are prevalent mainly during the spring and fall except for two episodes; one episode in July and the other in February. On some of the selected days such as March 15 and April 13, slight drizzle was indicated below the cloud base by radar echoes. Most cloud layers existed below 3 km above the ground level (AGL) except for October 6, when the cloud layer was well above the mixed layer (ML) determined from the vertical profile of potential temperature. The average thickness of the cloud layer was widely variable from 150 m to 1600 m. There was no appreciable precipitation at the surface during any of

the analysis periods. On November 6 only, there had been some rainfall during the previous night from 0900 ~ 1200 UTC (local time is 6 hours earlier than UTC).

Figure 2 presents the time series of cloud boundaries (cloud base and cloud top heights), total horizontal and diffuse irradiance from MFRSR, cloud fraction estimated from broadband shortwave radiometry, cloud optical depth (τ_c) and LWP, effective radius ($r_{e,M}$) evaluated by the Mie scattering retrieval, and aerosol scattering coefficient (σ_{sp}) for April 13, 2000. Values plotted for τ_c, LWP are 5-minute averages, and values of r_e are calculated from these 5-minute averages. The 5-minute averaging period permits the narrow field-of-view measurement of LWP to better correspond to the wide field-of-view measurement of τ_c by the MFRSR (Min et al., 2001). These data are presented in detail to illustrate the application of selection criteria for suitable cloud situations and analysis procedure as well as the evolution of cloud properties. As noted above, the method of determining τ_c presumes horizontal homogeneity. Satisfaction of this requirement is indicated by the temporal homogeneity of the several traces. A single cloud layer was well defined extending from 420 ± 90 m to 920 ± 120 m (unless otherwise specified, ± denotes standard deviation). The matching of total and diffuse irradiances from 1300 to 1840 UTC is further indication of total overcast conditions, confirmed by the cloud fraction VAP. Beginning about 1900 UTC, the cloud fraction began to depart from unity and thereafter decreased continuously to 0.2 around 2100 UTC. After 1840 UTC the total horizontal irradiance was about twice as great as the diffuse irradiance, and transmittance inferred from MFRSR began to increase substantially. The thick black line identifies the period that meets the criteria for determination of cloud optical depth, which we denote as the analysis period.

During the analysis period, τ_c and LWP tend to track each other over the course of the episode when plotted on a logarithmic scale, indicative of a relatively constant proportionality between them during the completely overcast period. Notably, τ_c from MFRSR and LWP from MWR exhibited similar fluctuations during the overcast situation, such that as LWP increases (decreases), optical depth similarly increases (decreases), despite being measured by completely different instruments with greatly different fields of view, 120° and 4.5°, respectively. Because of partly cloudy sky after 1840 UTC scattered variation was exhibited in apparent τ_c, and r_e was no longer considered valid. The retrieved scattered values of τ_c and r_e outside the analysis period are not included in the episode averages reported in Table 2.

Initially during the analysis period, τ_c and LWP remained relatively constant, decreasing slightly from 1300 to 1500 UTC. At about 1500 UTC, both τ_c and LWP increased by about a factor of 2; r_e decreased slightly from 6.8 ~ 7.2 μm to 5.8 ~ 6.5 μm coincident with a shift in surface wind from southeasterly (150° ~ 170°) to southwesterly (200°) associated with the passage of a cold front in association with an intensified trough, which developed southwestward from Canada. Intermittent drizzle was present from 1300 to 1500 UTC; the radar is highly sensitive to even slight drizzle. Examination of LWP during this period demonstrated that total LWP was not appreciably influenced by drizzle, and the retrieval of ground-based remote sensing appears to be effective despite the drizzle.

Time series of cloud boundaries, optical depth, LWP, effective radius, and scattering coefficient for another four days are presented in Figure 3. On March 15 (Figure 3a), a low-level warm cloud existed below 2 km the entire day with widely variable cloud thickness. The cloud fraction VAP was nearly unity throughout the period, indicating completely overcast cloudy sky from 1340 to 1730 UTC. As in Figure 2, τ_c and LWP exhibited similar fluctuation during the overcast period, with a roughly linear dependence of τ_c on LWP. The mixed layer height increased from 600 m (1750 UTC) to 1400 m (2031 UTC), based on the vertical profile of potential temperature (at 1428, 1750, 2031, and 2331 UTC, not shown). The sounding (1428 and 1750 UTC) indicated that the low-level stratus was rapidly advected northward at about 15 m s^{-1}. Until 1700 UTC, the cloud layer was confined to 1 km, and slight drizzle was observed from the radar reflectivity; afterwards the cloud base lifted to 1 km. Concurrent with this, τ_c and LWP decreased from 42 ~ 45 and 164 ~ 194 g m^{-2} to 13 ~ 17 and 61 ~ 82 g m^{-2}, respectively, commencing around 1700 UTC. The aerosol light scattering coefficient also began to decrease around 1700 UTC, when the mixed layer height increased. In contrast, no systematic variation of r_e was observed during this analysis period. After 1730 UTC, the measurements of apparent optical depth were quite scattered, consistent with the complete overcast requirement no longer being fulfilled. Cloud droplet effective radius was obtained sporadically around 2030 UTC and 2300 UTC for a short period of 20~30 minutes. Effective radii after 1800 UTC are not used for the analysis because the criterion for 2-hour persistence of overcast situation was not satisfied.

On April 15 (Figure 3b), thick clouds persisted during the daytime with an average thickness of 1600 m. The cloud fraction VAP indicated a completely overcast situation until 1900 UTC. Subsequently the cloud fraction decreased to 0.9, and thus this period is

not included in the further analysis. Optical depth showed relatively larger values (63 ± 27) than on the other days, and LWP was also larger (230 ± 100 g m^{-2}) but fluctuated substantially after 1900 UTC. As on March 15 (Figure 3a), τ_c and LWP consistently exhibited similar fluctuations. The effective radius did not show significant variation until 2000 UTC, after which the apparent r_e exhibited substantial fluctuation, possibly because of large spatial inhomogeneity or patchy cloud-free sky contributing to the radiometer signal.

On October 5 (Figure 3c), very thin and low-level clouds with the average thickness of 150 m were present from 430 to 580 m AGL; τ_c and LWP showed the highest values of 90 ± 20 and 440 ± 100 g m^{-2}, respectively, of all selected days. These high values are especially remarkable given the small thickness of the cloud layer during this period, about 150 m, indicative of an average cloud liquid water content of 2 ~ 3 g m^{-3}. During the daytime, northerly flow gradually increased up to 15 m s^{-1} in the lower layer from the surface to 1 ~ 1.5 km AGL. Prior to the analysis period around 1630 UTC, there seemed to be a discontinuity of the cloud layer, when both τ_c and LWP decreased substantially and cloud fraction also decreased to 0.8 over a 1-hour period.

On October 26 (Figure 3d), a low-level warm cloud below 1.5 km AGL persisted the entire day. Around 1600 ~ 1800 UTC, two adjacent layers seemed to exist, but radiatively these can be regarded as a single layer. As on other days, τ_c and LWP tended to track each other over the course of the day. Around 1500 ~ 1600 UTC, τ_c and LWP decreased by a factor of 3 and 2, respectively, and correspondingly r_e increased from 8~9 μm to 12 ~ 13 μm. After 1900 UTC partly cloudy sky was indicated by the cloud fraction VAP (0.6 ~ 0.9).

In summary, episode-average optical depth ranged from 18 to 90 and LWP from 90 to 440 g m^{-2}. Episode-average effective radii of cloud droplets $\overline{r_{e,M}}$ ranged from 5.6 to 12.3 μm (Table 2).

Also presented in Table 2 are episode-average values of effective radius $\overline{r_{e,r}}$ calculated by the ratio of LWP to τ_c, i.e., under the assumption that the Mie scattering efficiency is equal to 2. These values are systematically greater than those that explicitly account for Mie scattering efficiency: average 1.07, standard deviation 0.02.

Here comparisons of τ_c, LWP and r_e are presented with values obtained by an approach using broadband radiometry to determine τ_c [Dong et al., 2002]. The analysis period of that

study was limited to March 2000, when the ARM program conducted an intensive observation period (IOP) at the SGP site to obtain comprehensive ground- and satellite-based measurements of clouds in conjunction with in-situ aircraft measurement of cloud microphysical properties. March 15 and 19 of the present study are coincident with analysis days reported by Dong et al. [2002]. Comparisons of τ_c, LWP, and r_e for March 15 are presented in Figure 4. Optical depth from narrowband radiometry (this study) was systematically higher by about 20% than that from broadband radiometry [Dong et al., 2002]. A possible explanation for the difference could lie in the values of surface albedo employed in the retrievals. Cloud optical depth retrieved from measured transmittance using a surface albedo that is erroneously high compared to the actual surface albedo would be erroneously high; correspondingly, the use of too low a surface albedo in the retrieval would result in underestimation of optical depth. In the narrow-band retrieval at 415 nm the surface albedo employed in the retrieval is already quite low (0.036), so the retrieval cannot greatly overestimate the optical depth of the cloud on account of overestimating the surface albedo; as a measure of this sensitivity, if the actual surface albedo were 0, the overestimate of cloud optical depth arising from use of surface albedo of 0.036 in the retrieval would be only about 3% (optical depth 20, solar zenith angle 40˚). In contrast, the broadband retrieval must employ a wavelength-dependent surface albedo, which is substantial at longer wavelengths at which the solar power is greatest. A candidate cause of underestimate of cloud optical depth by the broadband approach is therefore use of an erroneously low value of surface albedo in the retrieval.

For the determination of LWP from microwave radiometry, Dong et al. [2002] used modified absorption models developed by Liljegren et al. [2001], which yielded values lower by ~ 10% than those obtained with the algorithm used here [Liljegren et al., 2000], but with similar temporal variation. Overall there was rather good agreement between the two approaches, with less than 10% difference between the effective radii.

5. Relationship between Optical Depth and LWP

The relationship between optical depth and LWP during the analysis period (duration indicated in Table 1) is examined in Figure 5 for 12 of the 13 selected episodes. The lines in the figures represent the dependence of τ_c on LWP (Eq. 6) for values of cloud droplet effective radius of 4, 8, 12, and 16 μm. These scatterplots of τ_c against LWP show the

controlling influence of LWP on τ_c. Optical depth exhibited a roughly linear dependence on LWP as expected, but with slopes that varied from day to day. To the extent that the data can be represented as a linear dependence on a line through the origin, then they are indicative of a single constant value of r_e; any scatter about such a line is indicative of departure from a constant r_e. Despite wide variation of LWP, even in 5-minute averages, the effective radius was quite constant on most days, evidently representing an inherent property of clouds; an almost linear dependence of τ_c on LWP was exhibited especially on the plots of February 18, March 19, April 13, and July 23, with relatively steeper slopes indicating the effective radius to be around 5.2 ~ 5.6 μm. This result suggests that the cloud is horizontally homogeneous, consisting of relatively uniform particles. In general, the greater the slope, the closer the data appear to cluster about a straight line. On April 13, a discontinuity is indicated around the τ_c value of 30. As noted above, the time series also indicated the abrupt change of τ_c and LWP around 1500 UTC in association with the frontal passage (Figure 2). Compared to other days, plots of data for October 6, October 26 and November 6 were rather widely scattered and do not conform to a well-defined value of r_e, perhaps indicative of temporally and therefore probably spatially inhomogeneous clouds with variable r_e and possibly associated with increase in measurement uncertainties with larger value of r_e as discussed in the Appendix.

Overall the plots showed greater slopes than those of marine clouds [Schwartz et al., 2002; Wetzel and Stowe, 1999], consistent with lower effective radii of droplets for midlatitude continental clouds in the Northern Hemisphere. Above all, the influence of LWP on τ_c is manifested in the strong dependence of τ_c on LWP.

To quantitatively examine the dependence of optical depth on LWP, we have fitted regression lines to the data for each of the days, under assumption of a linear proportionality (regression line forced through the origin). Table 3 presents $\overline{r_{e,m}}$ from the slope of τ_c vs. LWP (L), which is given as

$$\overline{r_{e,m}} = \frac{3}{2}\frac{1}{\rho_w m}, \tag{8}$$

where the slope (m) is the regression slope of fit of τ_c vs. LWP constrained to pass through the origin:

$$m = \frac{\sum L_i \tau_{ci}}{\sum L_i^2} = \frac{\sum L_i^2 (\tau_{ci} / L_i)}{\sum L_i^2}; \tag{9}$$

where τ_{ci} and L_i represent the individual measurements of cloud optical depth and LWP, respectively. Alternatively the quantity m may be viewed as an average of the ratio $m_i = \tau_{ci}/L_i$ weighted by the square of LWP, $w_i = L_i^2$. Such a weighting gives an estimate of the ratio τ_c/L that is free from possible undue influence of any measurements for which LWP is very low, as might result from simply averaging the quantity τ_{ci}/L_i itself.

Values for $\overline{r_{e,m}}$ determined in this way (Table 3) ranged from 5.2 to 14.9 μm and generally close to those for $\overline{r_{e,r}}$ and $\overline{r_{e,M}}$, the averages of r_e obtained by Eq 6 and by the Mie scattering retrieval, respectively, , without evident systematic difference. Additional averaging algorithms are presented in the Appendix. The close agreement of the results by the several averaging methods indicates that the averaged value of effective radius over the event is not highly sensitive to the averaging algorithm. In subsequent examination of relation between effective radius and other variables (refer to Appendix), we use values of $\overline{r_{e,M}}$ obtained from the Mie retrievals.

Recognition that m is a weighted sum allows its standard deviation to be evaluated as

$$S_m = \left(\frac{\sum L_i^2 (\tau_{ci} / L_i - m)^2}{\sum L_i^2} \right)^{1/2} = \left(\frac{\sum \tau_{ci}^2}{\sum L_i^2} - m^2 \right)^{1/2}, \tag{10}$$

and the resultant statistical uncertainty in $\overline{r_{e,m}}$ to be calculated by conventional uncertainty propagation.

In addition to this statistical uncertainty in r_e there is also contribution to uncertainty arising from propagated uncertainties in LWP and τ_c, as described in the Appendix. Knowledge of these uncertainties allows evaluation of the uncertainty associated with a single measurement of r_e, shown as a function of LWP and τ_c in Figure 6. This measurement uncertainty is greatest at high values of L/τ_c. Comparison with the scatter of the data in Figure 5 suggests that this measurement uncertainty may be responsible for the greater scatter of the measurement at high values of L/τ_c, i.e., in the lower right corner of the figure.

The regression of τ_c on LWP also allows determination of F, the fraction of the variance in τ_c that is attributable to variance in LWP. The fraction of the variance in optical depth that is explained by variance in LWP is evaluated as

$$F = \frac{S_0^2 - S_f^2}{S_0^2} = 1 - \frac{\sum(\tau_{ci} - mL_i)^2}{\sum(\tau_{ci} - \overline{\tau_c})^2} \tag{11}$$

where S_0 is the standard deviation of τ_c about its mean value and S_f is its standard deviation about regression line. This fractional variance is analogous to the familiar R^2, the square of the Pearson product-moment correlation coefficient in linear regression, except that it may assume negative values if the regression forced through the origin results in an increase in variance over that about the mean value.

This fraction is widely variable, ranging from –0.63 (i.e., the data are not well represented by a regression line forced through the origin) to 0.97. For six of the 13 episodes, the variance in LWP accounted for more than 90% or more of the variance in τ_c. However three episodes (10/05, 10/06, and 11/06), which exhibited scattered distribution, yielded values of F to be very low or negative, indicative of cloud events that do not appear to be well characterized by a small range of effective radius. For the data set as a whole (796 measurements), the variance in LWP accounted for around 63% of the variance in τ_c; the regression slope of 0.19 $(g\ m^{-2})^{-1}$ corresponds to a cloud droplet effective radius of 7.7 μm.

The relationship between cloud optical depth and LWP averaged over each of several episodes is presented in Figure 7. Despite the substantial variation of both quantities within individual episodes, episodes with greater average LWP exhibited greater average τ_c. The diagonal line represents the regression line for the event-average values of τ_c and LWP; the regression slope of 0.21 $(g\ m^{-2})^{-1}$ corresponds to a cloud droplet effective radius of 7.1 μm. Cloud episodes with average effective radius lower than this value, as indicated by the size of the marker, are above and to the left of the overall regression line and those with larger average effective radius are below and to the right of this line. These results are indicative of substantial differences in the relation between episode-average cloud optical depth and liquid water path that is a consequence of the different effective radius for the several episodes. While the regression on event-average LWP accounts for the great majority

(74%) of the variance in event-average optical depth, it is seen that assumption of a constant relation between τ_c and LWP would lead to departures from observations on specific days as great as 50%.

6. Relationship of Effective Radius to Aerosol

This section examines the relation between effective radius and aerosol scattering coefficient within the time series on several days and in day-to-day comparisons. It should be noted that the measurement site is in a remote rural area that is not subject to appreciable local emissions of aerosols contributing to the reported light scattering coefficient and to any modification of cloud properties; hence these aerosols are expected to be dominated by long-range transport from distant sources associated with large-scale air masses. Considerable day-to-day variation of r_e has already been noted. Aerosol light scattering coefficient (σ_{sp}), which would be linearly proportional to concentration of cloud condensation nuclei for aerosol size distributions having the same shape and composition, is used as a measure of loading of aerosol particles. Light scattering coefficient of submicrometer aerosol at the surface averaged over the several analysis periods (Table 2) ranged from 5.0 to 122 Mm^{-1} and was widely variable, compared with the long-term averages of this quantity at the SGP site of 37.6 ± 33.7 Mm^{-1} for 1997 to 2000 based on hourly averaged data [Delene and Ogren, 2002]. Very likely because of the depleted airborne aerosol after rainfall on November 6, σ_{sp} was the lowest (5.0 ± 1.4 Mm^{-1}) and r_e was the highest (12.3 ± 5.2 μm) on that day.

We first compare time series of cloud and aerosol properties during the individual events (Figures 2 and 3). The comparison shows little indication of systematic correlations between r_e and σ_{sp}; we restrict attention to the time series indicated by the thick black line signifying time periods where we are confident that the requirements for retrieval of τ_c by narrowband radiometry, and hence of r_e, are satisfied. On April 13 (Figure 2), r_e gradually decreased from 6.8 ~ 7.2 μm to 5.8 ~ 6.5 μm at about 1500 UTC while at the same time σ_{sp} decreased systematically from 67 Mm^{-1} to 36 Mm^{-1}, opposite to the direction expected if change in effective radius were related to change in aerosol concentration. The opposite situation is observed on April 15 (Figure 3b), with slight gradual increase in effective radius together with slight gradual decline in σ_{sp}. On October 5 (Figure 3c), prior to the gap in the aerosol measurements, there was a rather strong systematic decrease in σ_{sp} with no

indication of systematic change in r_e; following 2100 UTC σ_{sp} increased somewhat, again with no indication of changes in r_e. Finally on October 26 there was a rather abrupt change in r_e at 1830 UTC, possibly associated with change in cloud structure, with no indication of any change in scattering coefficient. These considerations suggest little if any correlation on a given day between r_e and σ_{sp} measured at the surface.

As noted on several of the analysis days, the systematic changes in r_e and σ_{sp} over the course of the episode were not consistent with the expectation that greater aerosol loading would result in a decrease in r_e. This departure from expectation might be associated with the vertical distribution of σ_{sp}. Insight into this vertical profile and whether the surface aerosol is representative of that at cloud altitude can be gained from the in-situ aerosol profile (IAP). Three IAP flights coincided with the selected analysis days, April 13, May 19 and October 6. Vertical distributions of σ_{sp} from IAP flights and potential temperature from BBSS in the afternoon of each of these days are shown in Figure 8. The red circles indicate σ_{sp} measured by nephelometer at the surface. On April 13, a strongly decoupled aerosol distribution was exhibited with a marked discontinuity at the top of the mixed layer (ML) with σ_{sp} decreasing from 70 ~ 80 Mm^{-1} to 2 ~ 10 Mm^{-1}. ML heights determined by the sounding of potential temperature were around 800 ~ 900 m. Although cloud in the layer of 700 ~ 1800 m had disappeared around 2100 UTC (Figure 2), at least the upper portion of the cloud for this period was not closely coupled to aerosol at the surface. In contrast, the vertical structure on May 19 indicated a well-mixed structure coupling the cloud layer at 600 ~ 1000 m above the ground during 1500 ~ 1930 UTC, and ML height was around 1 km at 2029 and 2331 UTC. Therefore, aerosol properties measured on the surface would be expected to be well associated with those in the cloud within the ML. Lastly on October 6, a cloud layer existed 2600 ~ 3300 m above the ground during 1700 ~ 2230 UTC, and mixed layer height was 900 ~ 1000 m. The agreement of σ_{sp} at the surface with the values in the cloud layer must be seen as fortuitous. For these reasons we do not expect strong association of r_e in cloud and σ_{sp} at the surface over the course of individual days, but rather look for possible association in comparison of the different days for which the aerosol both at the surface and at cloud altitude might be subject to similar changes due to the transport of different air masses.

We next examine the relation between r_e and σ_{sp} at the surface for the entire data set. Figure 9 indicates a general decrease in r_e with increasing σ_{sp}, as expected for the Twomey

mechanism. The figure also shows the relatively small variation of σ_{sp} (and to lesser extent r_e) over the course of any given day in comparison to the variation over the entire data set. A relation between r_e and σ_{sp}, decreasing r_e with increasing σ_{sp}, becomes discernible only when examining the entire data set. Exceptions to the general pattern include the data for October 26, for which examination of the meteorological situation shows that a mixed layer did not develop during the daylight hours, resulting in vertical decoupling of the cloud layer and the surface.

Following Feingold et al. [2001] we quantify the aerosol influence on cloud microphysical properties by the quantity *IE* (indirect effect), the negative of the slope of log r_e vs. log σ_{sp}.

$$IE = -d\log r_e / d\log \sigma_{sp} \tag{12}$$

For cloud droplet number concentration, N_{cd}, varying with aerosol particle number concentration N_{ap} as $N_{cd} = N_{ap}^{\alpha}$, then for other variables such as liquid water content and updraft velocity being equal, r_e is expected to vary as aerosol loading to the $\alpha/3$ power, resulting in $IE = \alpha/3$. As suggested by Twomey [1977, page 103], α is expected to be constrained between 0 and 1, leading to $0 \le IE \le 0.33$. A value of *IE* of zero would indicate no influence of aerosol loading on cloud effective radius, whereas a value of 0.33 would indicate linear proportionality between aerosol number concentration and cloud droplet number concentration, again other variables being equal. Based on rather heuristic arguments, Twomey suggested $\alpha \sim 0.7$, leading to $IE \sim 0.23$. For the data set as a whole we obtain $IE = 0.13 \pm 0.009$ (standard error; $R^2 = 0.24$). Such a value of R^2 suggests that about a quarter of the variation in r_e is associated with variation in the aerosol loading as measured by light scattering coefficient at the surface. The value of *IE* obtained in this way is comparable to values 0.12 ~ 0.38 obtained by Feingold et al. [2001] based on satellite measurements of effective radius and nearby aerosol optical depth for situations influenced by smoke from biomass burning in Brazil. Comparable and somewhat lower values of *IE*, 0.03 - 0.16, were obtained by Feingold et al. [2003] based on r_e determined by cloud radar and aerosol extinction coefficient determined by Raman Lidar at the SGP site. Considerably lower values of *IE* were obtained by Breon et al. [2002], 0.04 over land, based on global satellite measurements of r_e and aerosol index (a measure of light scattering

by submicrometer aerosol particles) in nearby upwind cloud-free air. In view of the fact that *IE* obtained from the present measurements was obtained by comparing results obtained on different days in different seasons and with different liquid water content, and undoubtedly with different aerosol size distributions as well, perhaps the numerical value obtained here should not be over-interpreted. Nonetheless the magnitude is broadly consistent with previous works and with expectation, strengthening the attribution of different effective radii from day to day to differences in the loading of ambient aerosol that served as nuclei for the droplets comprising the clouds present on those days.

7. Discussion

7.1. Influence of Micrometeorological Conditions

In addition to any influences on r_e from aerosol loading, cloud formation and microphysical properties are greatly influenced by larger-scale meteorological processes, especially insofar as local turbulent intensity may affect the supersaturation and activation of aerosol particles. To address these influences, we examine the relations of r_e with potential temperature gradient and wind shear below the cloud from the surface to cloud base, in the cloud layer from the cloud base to cloud top, and above the ML from the mixed layer top to 1 km above the ML (Figure 10). The cases shown in the figure represent all situations for which soundings were taken during overcast cloudy time satisfying the conditions required for determination of τ_c and r_e. Only 9 situations meet these criteria. No correlation was exhibited between potential temperature gradient and r_e (not shown here), or between vertical wind shear and r_e (Figure 10). However, vertical wind shear above the ML exhibited anti-correlation with r_e ($R^2 = 0.35$), and thus appears to have an influence on r_e. The association of lower effective radius with the higher wind shear would suggest greater ascent rate of air parcels in cloud, which might enhance the cloud supersaturation, increase N_{cd}, and decrease r_e. Such an influence of turbulence on N_{cd} has previously been demonstrated by Leaitch et al. [1996]. Overall, r_e exhibited appreciable correlation ($R^2 = 0.41$) with Richardson number, Ri (Eq. 1; Figure 10d) above the ML, where Ri is determined by mainly wind shear because of high thermal stability above the mixed layer. Correlation between r_e and Ri is evident only above the ML. As the mixed layer top is located midway in cloud layer or just above the ML, vertical entrainment and exchange through ML top could also be expected to be related to r_e.

7.2. Dependence of Reflectivity on Effective Radius

Here we examine the alteration of cloud reflectivity associated with day-to-day variations in r_e. Examples of plots of cloud-top spherical albedo versus LWP are shown in Figure 11, similar to those presented by Twomey [1977] and Schwartz et al. [2002]. We have used the individual measurements for the data points satisfying the selection criteria of Section 4. The cloud-top spherical albedo is calculated from the measured τ_c by Eq. 7. The clusters of data points exhibited apparent day-to-day differences with distinct segregation, manifesting the different dependencies on any given day. The curves shown in the figure represent the dependence of α_{sph} on LWP for average values of r_e calculated for each day, showing the increase in modeled spherical albedo with decreasing drop radius for a given LWP. The scatter of the data about the individual curves is indicative of the residual scatter for each day. Cloud albedo is most sensitive to LWP; much more variation in spherical albedo is attributable to variation in LWP than to day-to-day differences in r_e. Nonetheless the systematic difference in cloud top spherical albedo for a given LWP attributable to difference in r_e as determined by ground-based remote sensing is evident in the comparison of the data for the several days. Notably, the decrease in r_e results in marked increase in cloud albedo.

The change in broadband shortwave radiation budget (0.25 ~ 4 μm) associated with changes in r_e indicated in Figure 11 was evaluated using the SBDART radiation transfer model. For LWP = 100 g m^{-2}, the cloud optical depths for r_e equal to 10.2,7.8, and 5.8 μm are 15.1, 20.8 and 28.3, respectively. For solar zenith angle 60°, the corresponding calculated values of net broadband downwelling solar irradiance at the top of the atmosphere for surface albedo corresponding to a vegetated surface are 293, 266, and 240 W m^{-2}, respectively; that is a decrease in r_e from 10.2 to 5.8 μm and resultant increase in τ_c decreases the absorbed irradiance by 53 W m^{-2}. The magnitude of this effect, which is attributable solely to changes in r_e for realistic values of cloud LWP and other parameters, and likely a consequence of changes in aerosol loading, must be viewed as substantial in any quantitative consideration of the shortwave radiation budget locally and, by extension, globally.

8. Summary

Ground-based remote sensing of cloud optical depth and LWP has been used to determine the dependence of optical depth on LWP, using SGP ARM data archive for the entire year 2000. The characteristics of cloud droplet effective radius (r_e) and its relation to aerosol have also been investigated.

Optical depth and LWP showed wide variation on any given day, which represents an inherent property of clouds. However optical depth and LWP tend to closely track each other over the course of the episode, indicating a relatively linear dependence between them during the complete overcast situation, despite being measured by completely different instruments. The influence of LWP on cloud optical depth (τ_c) is clearly manifested in the strong dependence of τ_c on LWP. The variance in LWP is responsible for day-to-day variance in τ_c, accounting for about 63 % of the variance in optical depth for the whole data set. On a day-to-day basis, cloud droplet effective radius was found to exhibit negative correlation with σ_{sp} at the surface, as expected for the Twomey mechanism, although r_e appeared to be influenced as well by other factors such as vertical decoupling structure of aerosol and vertical wind shear. Notably, a decrease in r_e and the resultant enhancement of τ_c result in the increase in cloud albedo and decrease in absorption of solar radiation; for solar zenith angle 60° and LWP = 100 g m^{-2}, as effective radius decreases from 10.2 to 5.8 μm, as determined on different days, the resultant decrease in calculated net shortwave irradiance at the top of the atmosphere (Twomey forcing) is about 50 W m^{-2}.

Future work would be to examine how well surface aerosol measurements could represent the overlying atmospheric column, using in-situ aircraft measurement and Raman Lidar. Additionally the influence of turbulent factors and vertical entrainment on r_e should be investigated in more accurately quantifying the aerosol influence on cloud microphysics. More knowledge of these uncertainties is needed to improve understanding of aerosol indirect effects on radiation and climate.

Acknowledgments

We thank J. Ogren and P. Sheridan for 1-minute averages of σ_{sp} with IAP flight data, X. Dong and J. Liljegren for cloud optical depth and LWP for the comparison with this study, and C. Long for the information of the fractional sky cover. We thank two reviewers for

constructive criticism of the initial draft of this paper. This work was supported in part by US DOE's ARM program. B.-G. Kim was supported in part by Korean Science and Engineering Foundation.

Appendix. Statistics and Uncertainties

In order to compare values of effective radius from event to event it is necessary to average the measurements and to calculate uncertainties arising from propagated measurement uncertainty and statistical uncertainty over the events. While it is not straightforward to do this for effective radius $r_{e,M}$ obtained by the Mie retrieval method, it is relatively easy to obtain these uncertainty estimates for effective radius $r_{e,r}$ determined from the ratio of LWP to τ_c. For any individual determination of effective radius evaluated as (Eq. 6),

$$r_{e,i} = \frac{3}{2\rho}\frac{L_i}{\tau_i} \tag{A1}$$

there is an associated measurement uncertainty arising from uncertainties in the measurements of L_i and τ_i,

$$\delta(r_{e,i}) = \frac{3}{2\rho}\delta\left(\frac{L_i}{\tau_i}\right) \tag{A2}$$

where $\delta(L_i / \tau_i)$ is evaluated from the uncertainties in the individual measurements $\delta(\tau_i)$ and $\delta(L_i)$ by the usual rules for error propagation as

$$\delta\left(\frac{L_i}{\tau_i}\right) = \left(\frac{L_i}{\tau_i}\right)\left(\frac{\delta(\tau_i)}{\tau_i} \oplus \frac{\delta(L_i)}{L_i}\right) \tag{A3}$$

where the notation $x \oplus y$ denotes the square root of the sums of the squares $(x^2 + y^2)^{1/2}$.

For $\delta(L_i)$, we use the recommendation of Liljegren et al. [2001]; the root mean square accuracies of the retrievals are about 20 g m^{-2}, and 10% for cloud LWP below and above 200 g m^{-2}, respectively. The uncertainty in τ_c results from propagated uncertainty in transmittance T, which in turn results from uncertainty in measurements of instantaneous

irradiance, I and long-term average irradiance extrapolated to the top of the atmosphere by multiple Langley regressions, I_0. The fractional uncertainty in I_0 is estimated as 1% [Michalsky et al., 2001]. For the instantaneous irradiance, we take an uncertainty of 3%; the resulting uncertainty in T is therefore dominated by the uncertainty in I. From the linear relation between τ_c and $1/T$ in Figure 1b, it is readily established that the fractional uncertainty in τ_c is equal to fractional uncertainty in T and hence equal to the fractional uncertainty in I.

In principle the average effective radius over the event might be calculated as the simple average over the course of the event of the individual measurements of effective radius evaluated from the ratio of LWP to τ_c (Eq A1):.

$$\overline{r_{e,r}} = \frac{1}{n}\sum r_{e,i} \tag{A4}$$

where the sum is taken over the n individual measurements. This approach allows the statistical uncertainty – the standard deviation $S(\overline{r_{e,r}})$ and the standard error of the mean $sem(\overline{r_{e,r}})$ – to be calculated in the usual way. The propagated measurement uncertainty in $\overline{r_{e,r}}$ is estimated as

$$\delta(\overline{r_{e,r}}) = \frac{3}{2\rho}\frac{1}{n}\Sigma^{\oplus}\delta\left(\frac{L_i}{\tau_i}\right) \tag{A5}$$

The notation $\Sigma^{\oplus}$ is introduced to denote the square root of the sum of the squares, i.e.,

$$\Sigma^{\oplus} x_i \equiv \left(\sum {x_i}^2\right)^{1/2} \tag{A6}$$

Knowledge of $sem(\overline{r_{e,s}})$ and $\delta(\overline{r_{e,s}})$ allows the overall uncertainty (measurement uncertainty + statistical uncertainty) associated with $\overline{r_{e,s}}$ to be evaluated as

$$\Delta(\overline{r_{e,r}}) = \delta(\overline{r_{e,r}}) \oplus sem(\overline{r_{e,r}}) \tag{A7}$$

In the foregoing discussion it was implicitly assumed that the uncertainty associated with each of the measurements was the same and therefore that the average could be calculated by equally weighting each measurement. In the present situation, as the

measurement uncertainty $\delta(L_i / \tau_i)$ differs somewhat for each measurement we calculate the several average quantities as weighted averages

$$\overline{r_{\mathrm{e,w}}} = \frac{\sum w_i r_{\mathrm{e},i}}{\sum w_i} \tag{A8}$$

and

$$\delta(\overline{r_{\mathrm{e,w}}}) = \frac{3}{2\rho} \frac{\Sigma^{\oplus} w_i \delta\left(\frac{L_i}{\tau_i}\right)}{\sum w_i} \tag{A9}$$

where the weights w_i are taken as inversely proportional to the measurement uncertainty, i.e.,

$$w_i = 1/\left[\delta(L_i / \tau_i)\right]^2 \tag{A10}$$

In addition, overall uncertainty of $r_{\mathrm{e,w}}$ can be evaluated similarly as Eq. A8.

Calculation of $r_{\mathrm{e,m}}$ from the slope (m) of τ_{c} vs. LWP (L) is previously described in Eq. 8. As the measurement uncertainty $\delta(\tau_i / L_i)$ also differs somewhat for each measurement, we similarly calculate $\delta(m)$ as weighted averages (Eq. A11)

$$\delta(m) = \frac{\Sigma^{\oplus} {L_i}^2 \delta\left(\frac{\tau_i}{L_i}\right)}{\sum {L_i}^2} \tag{A11}$$

and $\Delta(m)$ as Eq. A7. Then, the overall uncertainty of $\overline{r_{\mathrm{e,m}}}$ is calculated as

$$\Delta(\overline{r_{\mathrm{e,m}}}) = \overline{r_{\mathrm{e,m}}} \frac{\Delta(m)}{m} \tag{A12}$$

A possible concern over these approaches is that r_{e} is an average of ratios. In general averaging of ratios is potentially dangerous in that the average can be dominated by a few terms having low values of the denominator (τ_i). In view of this concern an alternative

approach would be to evaluate the average effective radius over an event as the ratio of the time integrated quantities

$$\overline{r_{\mathrm{e,t}}} = \frac{3}{2\rho}\frac{\int L dt}{\int \tau dt} = \frac{3}{2\rho}\frac{\sum L_i}{\sum \tau_i} \tag{A13}$$

where the sum is taken over the measurements during the event. This approach readily allows a robust estimation of the event average.

The average effective radii for the several events as calculated by these four approaches are presented in Table A1 and Figure A1, along with the uncertainties. Average values of effective radius calculated by all approaches are similar, lending confidence to the average of ratios approach. However the ratio of integrals approach does not readily allow evaluation of the associated uncertainty, especially as the standard deviations of numerator and denominator in $r_{\mathrm{e,t}}$ are dominated by fluctuations in L and τ, which are much greater than fluctuations in r_{e}.

Comparison of the event-average effective radii in Table A1 indicates not only that the average values for the several events differ substantially from day to day but also that the differences in r_{e} for the several events are substantially greater than the uncertainty in r_{e} due to either measurement uncertainty or statistical uncertainty (Figure A1). Values of each average of r_{e} obtained for the several events agree closely with one another. Therefore, for subsequent analysis values of r_{e} were taken as the simple average of the average of the individual measurements obtained by the Mie scattering retrieval $\overline{r_{\mathrm{e,M}}}$.

References.

Ackerman, A.S., O.B. Toon, D.E. Stevens, A.J. Heymsfield, V. Ramanathan, and E.J. Welton, Reduction of tropical cloudiness by soot, *Science, 288*, 1042-1047, 2000.

Ackerman, T.P., G.M. Stokes, The Atmospheric Radiation Measurement Program, *Physics Today*, 38-44, 2003.

Albrecht, B.A., Aerosols, cloud microphysics, and fractional cloudiness, *Science, 245*, 1227-1230, 1989.

Albrecht, B.A., C.S. Bretherton, D. Johnson, W.H. Schubert, and A.S. Frisch, The Atlantic Stratocumulus Transition Experiment – ASTEX. *Bull. Amer. Meteor. Soc., 76*, 889-904, 1995.

Anderson, T.L., J.A. Ogren, Determining aerosol radiative properties using the TSI 3563 integrating nephelometer, *Aerosol Sci. Technol., 29*, 57-69, 1998.

Bevington, P.R., *Data reduction and error analysis for the physical sciences*, Mc-Graw-Hill, New York, 1969.

Breon, F.-M., D. Tanre, and S. Generoso, Aerosol effect on cloud droplet size monitored from satellite, *Science, 295*, 834-838, 2002.

Brenguier, J.-L., H. Pawlowska, L. Schuller, R. Preusker, J. Fischer, and Y. Fouquart, Radiative properties of boundary layer clouds: droplet effective radius versus number concentration, *J. Atmos., Sci., 57*, 803-821, 2000

Charlson, R.J., S.E. Schwartz, J.M. Hales, R.D. Cess, J.A. Coakley Jr., J.E. Hansen, and D.J. Hofmann, Climate forcing by anthropogenic aerosols, *Science, 255*, 423-430, 1992.

Clothiaux, E.E., T.P. Ackerman, G.G. Mace, K.P. Moran, R.T. Marchand, M.A. Miller, and B.E. Martner, Objective determination of cloud heights and radar reflectivities using a combination of active remote sensors at the ARM CART sites, *J. Appl. Met., 39*, 645-665, 2000.

Delene, D.J., and J.A. Ogren, Variability of aerosol optical properties at four North American surface monitoring sites, *J. Atmos., Sci., 59*, 1135-1150, 2002.

Dong, X., P. Minnis, G. Mace, W. Smith Jr, M. Poellot, R. Marchand, A. Rapp, Comparison of stratus cloud properties deduced from surface, GOES, and aircraft data during the March 2000 ARM cloud IOP, *J. Atmos., Sci., 23*, 3265-3284, 2002.

Dong, X., T.P. Ackerman, E.E. Clothiaux, P.Pilewskie, and Y. Han, Microphysical and radiative properties of boundary layer stratiform clouds deduced from ground-based measurements, *J. Geophys. Res., 102,* 23829-23843, 1997.

Dong, X., T.P. Ackerman, E.E. Clothiaux, Parameterization of microphysical and shortwave radiative properties of boundary layer stratus from ground-based measurements, *J. Geophys. Res., 103,* 31681-31693, 1998.

Feingold, G., W. Eberhard, D.E. Lane, and M. Previdi, First measurements of the Twomey effect using ground-based remote sensors, *Geophys. Res. Lett., 30(6)*, 1287, doi:10.1029/2002GL016633, 2003..

Feingold, G., L.A. Remer, J. Ramaprasad, and Y. Kaufman, Analysis of smoke impact on clouds in Brazilian biomass burning regions: An extension of Twomey's approach, *J. Geophys. Res., 106,* 22907-22922, 2001.

Han, Q., W.B. Rossow, and A.A. Lacis, Near-global survey of effective droplet radii in liquid water clouds using ISCCP data, *J. Climate*, 7, 465-497, 1994.

Han, Q., W.B. Rossow, J. Chou, and R.M. Welch, Global variation of column droplet concentration in low-level clouds, *Geophys. Res. Lett., 25,* 1419-1422, 1998.

Hansen, J.E., M. Sato, and R. Ruedy, Radiative forcing and climate response, *J. Geophys. Res., 102*, 6831-6864, 1997.

Hansen J. E. and Travis L. D., Light-scattering in planetary atmospheres. *Space Sci. Rev. 16*, 527-610, 1974.

Harrison, L.C., and J.J. Michasky, Objective algorithms for the retrieval of optical depths from ground-based measurements, *Appl. Optics, 33,* 5126-5132, 1994.

Harrison, L.C., J. Michalsky, and J. Berndt, Automated multifilter rotating shadow-band radiometer: an instrument for optical depth and radiation measurements, *Appl. Optics, 33*, 5118-5125, 1994.

Harshvardhan, S.E. Schwartz, C.E. Benkovitz, and G. Guo, Aerosol influence on cloud microphysics examined by satellite measurements and chemical transport modeling, *J. Atmos. Sci., 59,* 714-725, 2002.

Harshvardhan, and M.D. King, Comparative accuracy of diffusive radiative properties computed using selected multiple scattering approximations, *J. Atmos. Sci., 50*, 247-259, 1993.

Hu, Y.X., and K. Stamnes, An accurate parameterization of the radiative properties of water clouds suitable use of in climate models, *J. Climate, 6*, 728-742, 1993.

International Panel on Climate Change, *Climate change 2001: the scientific basis,* Cambridge University Press, 2001.

Kiehl, J.T., and B.P. Briegleb, The relative roles of sulfate aerosols and greenhouse gases in climate forcing, *Science, 260*, 311-314, 1993.

Leaitch, W.R., C.M. Banic, G.A. Isaac, M.D. Couture, P.S.K. Liu, I. Gultepe, S.-M. Li, L. Kleinman, P.H. Daum, J.I. MacPherson, Physical and chemical observations in marine status during the 1993 North Atlantic Regional Experiment: Factors controlling cloud droplet number concentrations, *J. Geophys. Res., 101*, 29123-29135, 1996.

Leontieva, E., and Stamnes, K., Remote sensing of cloud optical properties from ground-based measurements of transmittance: A feasibility study, *J. Appl. Meteor., 35*, 3011-2022, 1996.

Liljegren, J.C., Automatic self-calibration of ARM microwave radiometers, *Microwave Radiometry and Remote Sensing of the Earth's Surface and Atmosphere*, P.Pampaloni and S. Paloscia, Eds. VSP Press, 433-441, 2000.

Liljegren, J.C., E.E. Clothiaux, G.G. Mace, S. Kato, X. Dong, A new retrieval for cloud liquid water path using a ground-based microwave radiometer and measurements of cloud temperature, *J. Geophys. Res., 106,* 14485-14500, 2001.

Li, Z., A. P. Trishchenko, H. W. Barker, G. L. Stephens, and P. Partain, Analyses of Atmospheric Radiation Measurement (ARM) program's Enhanced Shortwave Experiment (ARESE) multiple data sets for studying cloud absorption. *J. Geophys. Res., 104,* 19127-19134, 1999.

Liu, Y., and P.H. Daum, Indirect warming effect from dispersion forcing, *Nature, 419*, 580-581, 2002.

Long, C.N. and T.P. Ackerman, Identification of Clear Skies from Broadband Pyranometer Measurements and Calculation of Downwelling Shortwave Cloud Effects, *J. Geophys. Res., 105*, 15609-15626, 2000.

Marshak, A., Y. Knyazikhan, A.B. Davis, W.J. Wiscombe, and P. Pilewskie, Cloud-vegetation interaction: using of normalized difference cloud index for estimation of cloud optical thickness, *Geophys. Res. Lett., 27,* 1695-1698, 2000.

Michalsky, J.J., J.A. Schlemmer, W.E. Berkheiser, J.L. Berndt, L.C. Harrison, N.S. Laulainen, N.R. Larson, and J.C. Barnard, Multiyear measurements of aerosol optical depth in the Atmospheric Radiation Measurement and quantitative links programs, *J. Geophys. Res., 106*, 12099-12107, 2001.

Min, Q., and L.C. Harrison, An adjoint formulation of the radiative transfer method, *J. Geophys. Res., 101*, 1635-1640, 1996a.

Min, Q., and L.C. Harrison, Cloud properties derived from surface MFRSR measurements and comparison with GEOS results at the ARM SGP site, *Geophys. Res. Lett., 23*, 1641-1644, 1996b.

Min, Q.-L., L. C. Harrison, and E. Clothiaux, Joint statistics of photon pathlength and cloud optical depth: case studies, *J. Geophys. Res., 106*, 7375-7386, 2001.

Nakajima, T., A. Higurashi, K. Kawamoto, J.E. Penner, A possible correlation between satellite-derived cloud and aerosol microphysical parameters, *Geophys. Res. Lett., 28*, 1171-1174, 2001.

Radke, L.F., J.A. Coakley Jr., and M.D. King, Direct and remote sensing observations of the effects of ships on clouds, *Science, 246*, 1146-1149, 1989.

Ricchiazzi, P., S. Yang, C. Gautier, and D. Sowie, SBDART: A research and teaching software tool for plane-parallel radiative transfer in the Earth's atmosphere, *Bull. Amer. Meteorol. Soc., 79,* 2101-2114, 1998.

Schwartz, S.E., Harshvardhan, and C.M. Benkovitz, Influence of anthropogenic aerosol on cloud optical depth and albedo shown by satellite measurements and chemical transport modeling, *PNAS, 99*, 1784-1789, 2002.

Schwartz, S.E., and A. Slingo, Enhanced shortwave cloud radiative forcing due to anthropogenic aerosols, *Clouds, Chemistry and Climate*, Edited by P.J. Crutzen and Ramanathan, 191-236, 1996.

Sheridan, P.J., D.J. Delene, and J.A. Ogren, Four year of continuous surface aerosol measurements from the Department of Energy's Atmospheric Radiation Measurement program Southern Great Plains cloud and Radiation testbed site, *J. Geophys. Res., 106*, 20735-20747, 2001.

Slingo, A., A GCM parameterization for the shortwave radiative properties of water clouds, *J. Atmos. Sci., 46*, 1419-1427, 1989.

Stamnes, K., S. Tsay, W. Wiscombe, and K. Jayaweera, Numerically stable algorithm for discrete-ordinate-method radiative transfer in multiple scattering and emitting layered media. *Appl. Opt., 27*, 2502–2509, 1988.

Stephens, G.L., The parameterization of radiation for numerical weather prediction and climate models, *Mon. Wea. Rev., 112*, 826-867, 1984.

Stokes, G.M., and S.E. Schwartz, The Atmospheric Radiation Measurement (ARM) Program: Programmatic background and design of the cloud and radiation testbed, *Bull. Am. Meteorol. Soc., 75,* 1201-1221, 1994.

Stull, R.B., *An introduction to boundary layer meteorology*, Kluwer Academic Publishers, Dordrecht, 1997.

Twomey, S., The influence of pollution on the shortwave albedo of clouds, *J. Atmos. Sci., 34*, 1149-1152, 1977.

van de Hulst, H. C. *Light Scattering by Small Particles*. New York: Dover, 1981

Wetzel, M.A., and L.L. Stowe, Satellite-observed patterns in stratus microphysics, aerosol optical thickness, and shortwave radiative forcing, *J. Geophys. Res., 104*, 31287-31229, 1999.

Figure Captions

Figure 1. (a) Calculated atmospheric transmittance as a function of cloud optical depth, evaluated as ratio of downwelling irradiance at surface to that at top of atmosphere. (b) Calculated dependence of cloud optical depth as a function of inverse of atmospheric transmittance; lines in (b) connecting points for which calculations were made show near linear dependence of the relation. Wavelength band 0.39 - 0.43 μm; solar zenith angle θ_0 40˚ and 70˚; cloud-base height 2 km; surface albedo 0.04; atmospheric water vapor column 2.9 g cm^{-2}; cloud droplet effective radius 8 μm and 12 μm. Calculated with SBDART [Ricchiazzi et al., 1998; http://arm.mrcsb.com/sbdart].

Figure 2. Time series of cloud boundaries (cloud base and cloud top heights), total horizontal and diffuse irradiances, atmospheric transmittance, cloud optical depth (τ_c), LWP, effective radius of cloud droplets (r_e) and aerosol scattering coefficient (σ_{sp}) on April 13, 2000. Thick black line indicates the period that satisfies the selection criteria for further analysis.

Figure 3. Time series of cloud boundaries, cloud optical depth (τ_c), LWP, effective radius of cloud droplets (r_e) and aerosol scattering coefficient (σ_{sp}) on the days of (a) March 15, (b) April 15, (c) October 05, and (d) October 26, 2000. Thick black line indicates the further analysis period.

Figure 4. Comparisons of (a) cloud optical depth, (b) LWP, and (c) effective radius on March 15, 2000 with values reported by Dong et al. [2002] for which optical depth was obtained from broadband radiometry and LWP was obtained by the algorithm of Liljegren et al. [2001].

Figure 5. Scatterplots of cloud optical depth (τ_c) against cloud LWP for the analysis period on the different days. Lines denote cloud optical depth for indicated constant values of effective radius, r_e. Scatterplot for April 23, similar to others shown, is omitted from the figure for compactness of presentation.

Figure 6. Measurement uncertainties $\delta(\overline{r_e})$ associated with a single measurement of r_e as a function of τ_c and LWP. These uncertainties pertain to retrieval of r_e by equation 6.

Figure 7. Scatterplot of event-average cloud optical depth (τ_c) against event-average cloud LWP. Radius of filled circles is proportional to effective radius, and error bar indicates 2 times overall uncertainties of cloud optical depth and LWP, respectively. The regression

slope of event-average τ_c vs. event-average LWP constrained through the origin is 0.21 corresponding to r_e of 7.1 μm, and the fraction of the variance (F) in τ_c associated with the regression is 0.74.

Figure 8. Vertical profiles of aerosol scattering coefficients from in-situ Aerosol Profile (IAP) flights and potential temperature from Balloon-Borne Sounding System (BBSS) on April 13, May 19, and October 6, 2000. Red circle indicates the aerosol scattering coefficient measured at the surface.

Figure 9. Scatterplot (logarithmic axes) of 5-minute average cloud-drop effective radius (r_e) vs. light scattering coefficient for submicrometer aerosol at 550 nm (σ_{sp}). Data for individual days are distinguished by color and symbol. Equation of regression is $\log r_e = 1.06 - 0.13 \log\sigma_{sp}$; $R^2 = 0.24$. Data for σ_{sp} are interpolated to measurement time of r_e, and gaps in σ_{sp} (but not r_e) are filled by interpolation.

Figure 10. Scatterplots of effective radius versus vertical wind shear for the different layers, (a) below the cloud from the surface to cloud base, (b) in the cloud layer from the cloud base to cloud top and (c) above the mixed layer from the mixed layer to 1 km above the ML top ($R^2 = 0.35$). (d) Scatterplots of effective radius versus logarithm (base 10) of the Richardson number (Ri) above the mixed layer only ($R^2 = 0.41$).

Figure 11. Cloud top spherical albedo as a function of cloud LWP calculated for measured LWP and τ_c for February 18, May 19 and October 21. Curves denote cloud albedo for indicated constant values of effective radius, r_e.

Figure A1. Comparison of alternative approaches to evaluating episode-average cloud drop effective radius: $r_{e,M}$, from Mie scattering retrieval; $r_{e,w}$, weighted average of individual measurements of effective radius; $r_{e,m}$, effective radius obtained from the slope of optical depth vs. LWP, $r_{e,t}$, ratio of time average LWP to time average optical depth,; and $r_{e,r}$, average of measurements of effective radius evaluated from ratio of LWP to τ_c,; , all presented in order of increasing value of $r_{e,t}$. Error bars indicate the overall uncertainties of indicated quantities.

Table 1. Summary of primary instrumentation and value-added products[a].

Instrument	Measured Quantities	Comments	Temporal resolution	References
MFRSR (Multi-Filter Rotating Shadowband Radiometer)	Cloud optical depth (τ_c)	Measures direct and total-horizontal irradiances at 415 nm.	20 s	Min and Harrison [1996]
MWR (Microwave Radiometer)	Liquid water path (LWP)	Uses microwave brightness temperature, Accuracy 30 g m^{-2}	20 s	Liljegren [2000]
Nephelometer	Scattering coefficient (σ_{sp}) *	At 450, 550, 700 nm for the size of aerodynamic diameter less than 1μm	1 min	Sheridan et al. [2001]; http://www.cmdl.noaa.gov/ aero/data/.
ARSCL (Active Remotely-Sensed Cloud Locations)	Cloud boundaries	Best estimates from MMCR, Ceilometer and Lidar	10 s	Clothiaux et al. [2000]
BBSS (Balloon-Borne Sounding System)	Temperature (T), Relative Humidity (RH), wind speed (WS)	Sounding at 6 hour intervals (3 hour interval for Intensive Observation Period)	10 s	www.arm.gov/docs/instruments/static/bbss.html

[a] Value-added products refer to data sets resulting from assimilation and analysis of data from multiple instruments.

* IAP(In-situ Aerosol Profiling) measures vertical distributions of σ_{sp} 2-3 times a week.

Data are from www.archive.arm.gov except where indicated.

Table 2. Episode-average cloud and aerosol properties for each analysis period.

Date 2000	Duration UTC	Number of data n	Cloud layer height, m					LWP g m^{-2}		Optical Depth		Effective radius[1] µm		Effective radius[2] µm		σ_{sp} (550 nm) Mm^{-1}	
			Base		Top		Depth										
			$\overline{B}$	$S(B)$	$\overline{T}$	$S(T)$		$\overline{L}$	$S(L)$	$\overline{\tau_c}$	$S(\tau_c)$	$\overline{r_{e,M}}$	$S(r_{e,M})$	$\overline{r_{e,r}}$	$S(r_{e,r})$	$\overline{\sigma_{sp}}$	$S(\sigma_{sp})$
02/18	14:20-23:00	106	220	130	1070	220	850	143	55	41.5	17.6	5.8	0.7	5.3	0.6	73.7	10.5
03/15	13:40-17:30	48	180	80	890	170	710	158	55	32.4	9.4	7.8	0.9	7.2	0.9	67.9	6.9
03/19	13:40-17:00	41	410	50	920	180	510	109	50	31.8	15.0	5.6	0.6	5.2	0.5	28.3	2.3
04/13	13:00-18:40	69	420	90	920	120	500	101	35	27.1	10.2	6.1	0.7	5.7	0.6	50.5	25.7
04/15	13:00-18:45	70	200	140	1810	170	1610	231	99	62.7	27.0	6.0	0.6	5.6	0.6	100.2	22.3
04/23	14:00-16:15	28	500	170	1310	310	810	125	101	29.1	15.1	6.6	1.7	6.0	1.8	32.8	1.9
05/19	15:00-20:45	68	630	320	1060	310	430	133	114	26.8	18.0	7.8	2.0	7.1	2.2	19.1	9.9
07/23	13:00-16:45	48	200	100	740	130	540	124	57	34.4	15.4	5.8	0.5	5.4	0.5	45.5	4.8
10/05	18:30-23:00	54	430	60	580	70	150	439	102	89.8	20.5	7.9	1.7	7.5	1.9	13.5	5.1
10/06	17:10-23:00	69	2660	250	3330	200	670	91	36	17.8	4.1	8.1	1.9	7.5	2.0	10.2	1.1
10/21	13:45-19:30	65	330	160	1080	390	750	146	79	32.3	20.4	7.8	1.4	7.2	1.2	122.0	14.7
10/26	14:20-19:00	51	240	150	910	330	670	291	116	46.9	22.7	10.2	1.6	9.9	1.9	65.4	2.3
11/06	15:15-22:00	79	500	230	790	160	290	236	153	29.4	10.4	12.3	5.2	11.9	5.4	5.0	1.4

S indicates the standard deviation for indicated quantity; overbar indicates event-average; n indicates number of observations (5-minute averages of cloud properties during the episode) and does not pertain to aerosol measurements.

[1] Effective radius obtained from the Mie scattering retrieval.

[2] Effective radius obtained by the ratio method (eq 6). i.e., Q_e=2.

Table 3. Episode-average values of slope (m) of optical depth vs. LWP, the fraction (F) of the variance in optical depth explained by variance in LWP, and several measures of effective radius: $\overline{r_{e,M}}$ denotes average effective radius determined from the Mie scattering retrieval; $\overline{r_{e,r}}$ denotes average effective radius determined from the ratio of LWP to τ_c, Eq (6), and $\overline{r_{e,m}}$ denotes average effective radius determined from the slope m.

Date 2000	Duration UTC	m $(g\ m^{-2})^{-1}$	F	$\overline{r_{e,m}}$ μm	$\overline{r_{e,r}}$ μm	$\overline{r_{e,M}}$ μm
02/18	14:20-23:00	0.29	0.96	5.2	5.3	5.8
03/15	13:40-17:30	0.20	0.81	7.5	7.2	7.8
03/19	13:40-17:00	0.29	0.97	5.2	5.2	5.6
04/13	13:00-18:40	0.27	0.93	5.6	5.7	6.1
04/15	13:00-18:45	0.27	0.93	5.6	5.6	6.0
04/23	14:00-16:15	0.20	0.62	7.6	6.0	6.6
05/19	15:00-20:45	0.18	0.67	8.6	7.1	7.8
07/23	13:00-16:45	0.27	0.97	5.6	5.4	5.8
10/05	18:30-23:00	0.20	0.03	7.5	7.5	7.9
10/06	17:10-23:00	0.18	-0.28	8.3	7.5	8.1
10/21	13:45-19:30	0.23	0.96	6.6	7.2	7.8
10/26	14:20-19:00	0.16	0.84	9.2	9.9	10.2
11/06	15:15-22:00	0.10	-0.64	14.9	11.9	12.3

Table A1. Event-average values of effective radius and corresponding uncertainties obtained by the several averaging methods; effective radius from the ratio of the time-average LWP to time average optical depth, $\overline{r_{e,t}}$; simple average of individual measurements of effective radius obtained by the Mie method, $\overline{r_{e,M}}$; simple average of individual measurements of effective radius by the ratio of LWP to τ_c, $\overline{r_{e,r}}$; weighted average of individual measurements of effective radius, $\overline{r_{e,w}}$; effective radius obtained from the slope of optical depth vs. LWP, $\overline{r_{e,m}}$ (Unit: μm).

Date 2000	$\overline{r_{e,t}}$	$\overline{r_{e,M}}$	$\Delta(\overline{r_{e,M}})$	$\overline{r_{e,r}}$	$\Delta(\overline{r_{e,r}})$	$\overline{r_{e,w}}$	$\delta(\overline{r_{e,w}})$	$\Delta(\overline{r_{e,w}})$	$\overline{r_{e,m}}$	$\Delta(\overline{r_{e,m}})$
02/18	5.3	5.8	0.10	5.3	0.09	5.6	0.11	0.12	5.2	0.12
03/15	7.3	7.8	0.15	7.2	0.14	7.7	0.18	0.22	7.5	0.23
03/19	5.2	5.6	0.14	5.2	0.13	5.5	0.17	0.18	5.2	0.18
04/13	5.6	6.1	0.10	5.7	0.10	5.9	0.15	0.17	5.6	0.16
04/15	5.5	6.0	0.09	5.6	0.08	5.8	0.09	0.12	5.6	0.13
04/23	6.3	6.6	0.30	6.0	0.30	6.4	0.22	0.35	7.6	0.50
05/19	7.4	7.8	0.36	7.1	0.37	7.5	0.17	0.23	8.6	0.41
07/23	5.4	5.8	0.12	5.4	0.12	5.8	0.15	0.16	5.4	0.16
10/05	7.3	7.9	0.23	7.5	0.26	7.5	0.11	0.20	7.5	0.26
10/06	7.7	8.1	0.25	7.5	0.25	8.0	0.22	0.32	8.3	0.36
10/21	6.8	7.8	0.20	7.2	0.17	7.1	0.15	0.21	6.6	0.19
10/26	9.3	10.2	0.24	9.9	0.26	9.5	0.17	0.29	9.2	0.30
11/06	12.0	12.3	0.59	11.9	0.61	10.5	0.18	0.48	14.9	0.83

Δ denotes overall uncertainty; δ measurement uncertainty.

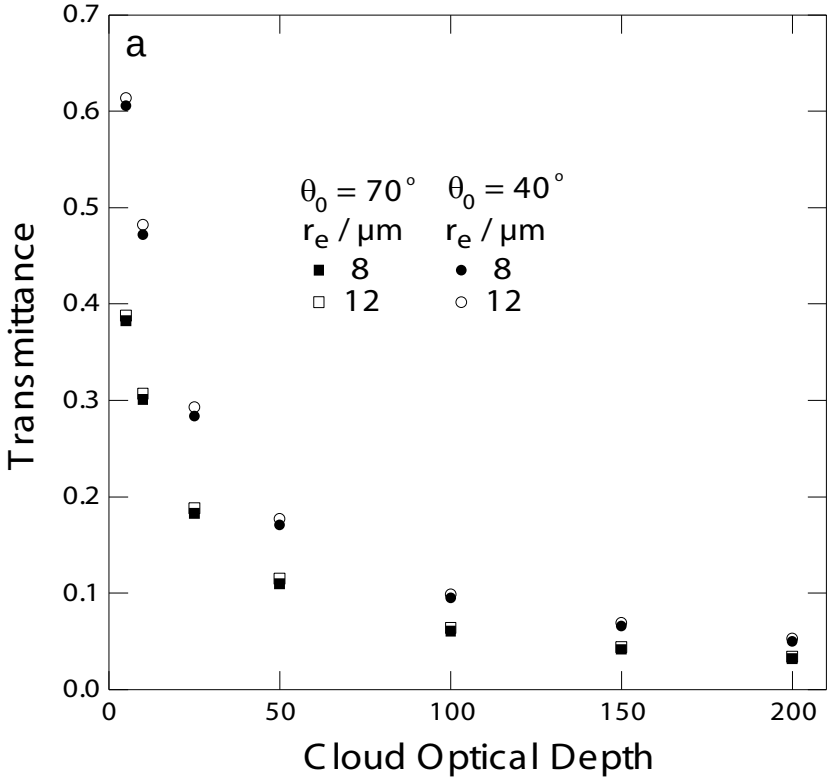
a
Transmittance
Cloud Optical Depth
θ0 = 70°
re / μm
8
12
θ0 = 40°
re / μm
8
12
0.0
0.1
0.2
0.3
0.4
0.5
0.6
0.7
0
50
100
150
200

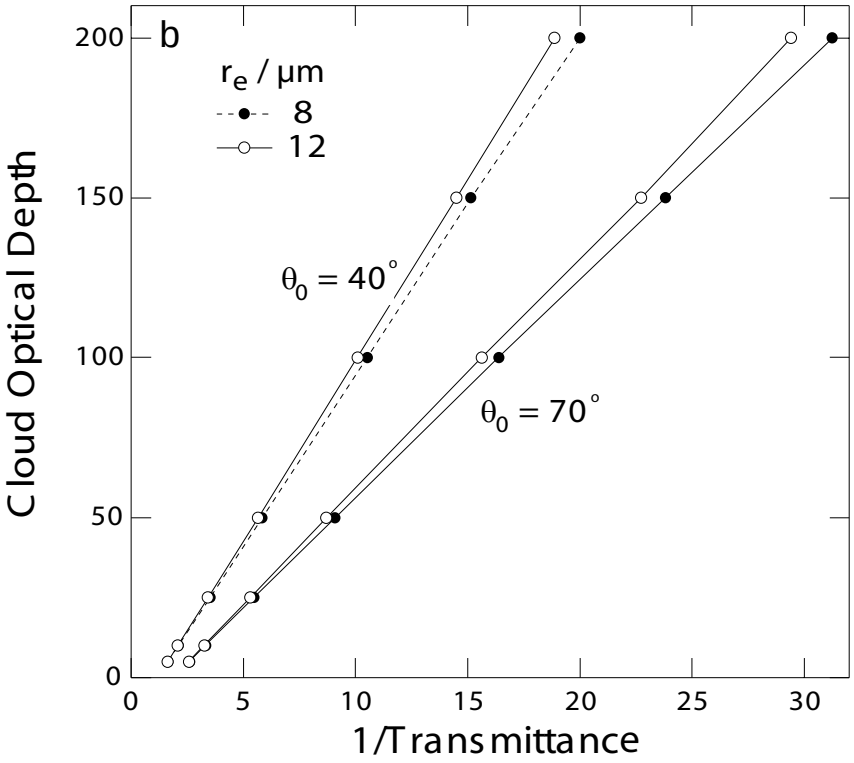
b
Cloud Optical Depth
1/Transmittance
re / μm
8
12
θ0 = 40°
θ0 = 70°
0
50
100
150
200
0
5
10
15
20
25
30

Figure 1

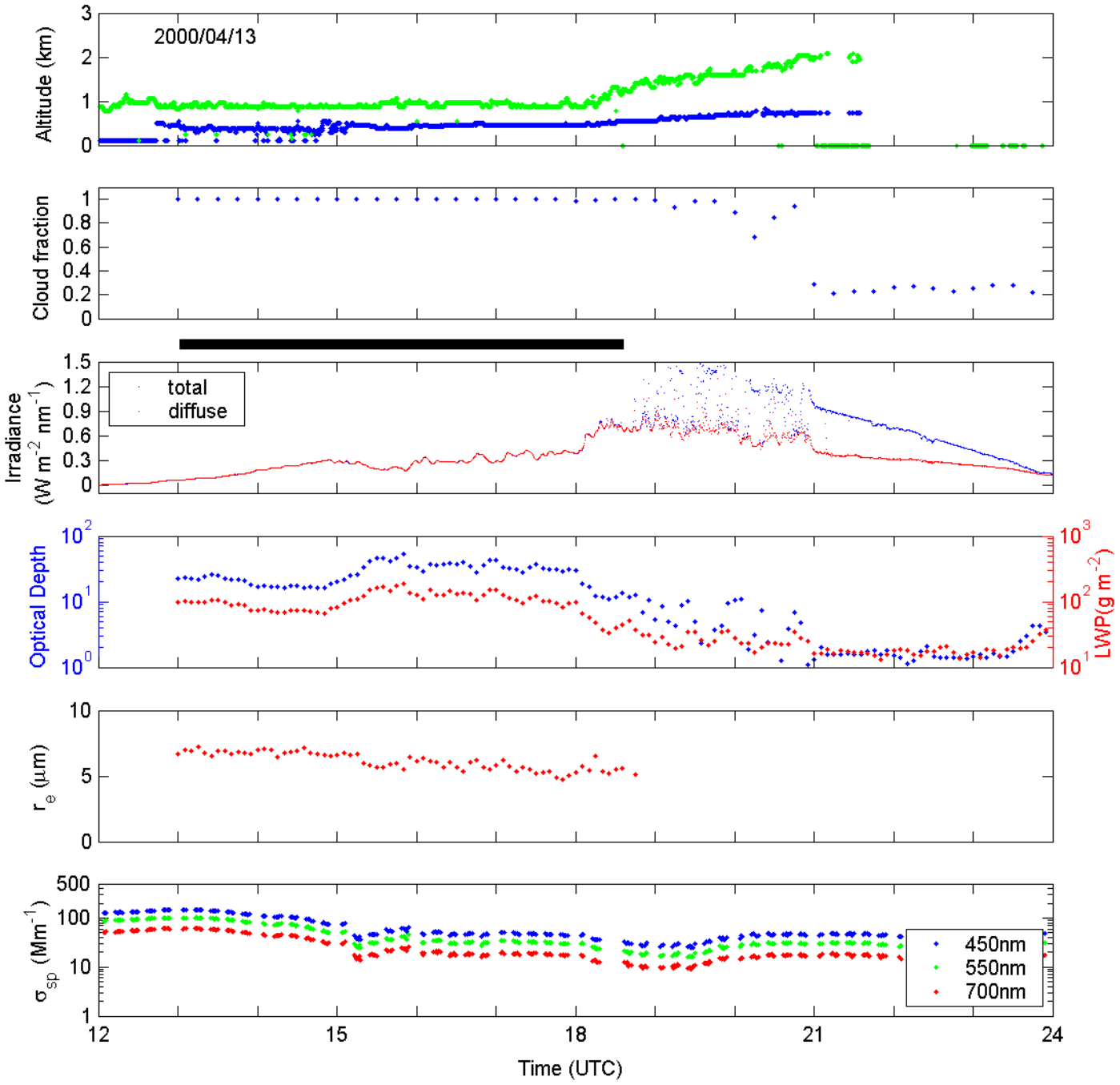
2000/04/13
Altitude (km)
Cloud fraction
Irradiance (W m-2 nm-1)
total
diffuse
Optical Depth
LWP(g m-2)
re (μm)
σsp (Mm-1)
450nm
550nm
700nm
Time (UTC)

Figure 2

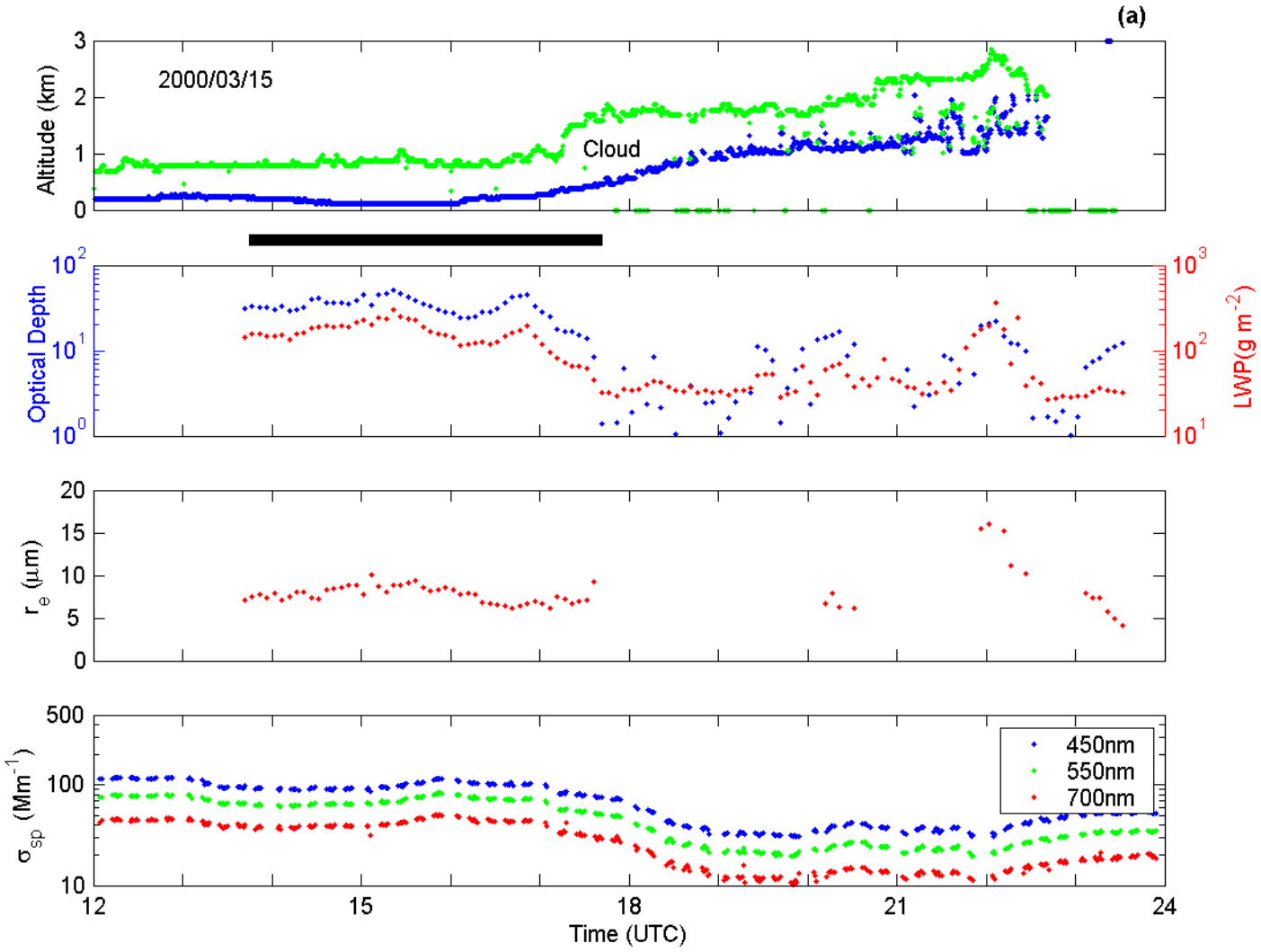
(a)
2000/03/15
Cloud
Altitude (km)
Optical Depth
LWP(g m^{-2})
r_e (μm)
σ_{sp} (Mm^{-1})
450nm
550nm
700nm
Time (UTC)

Figure 3

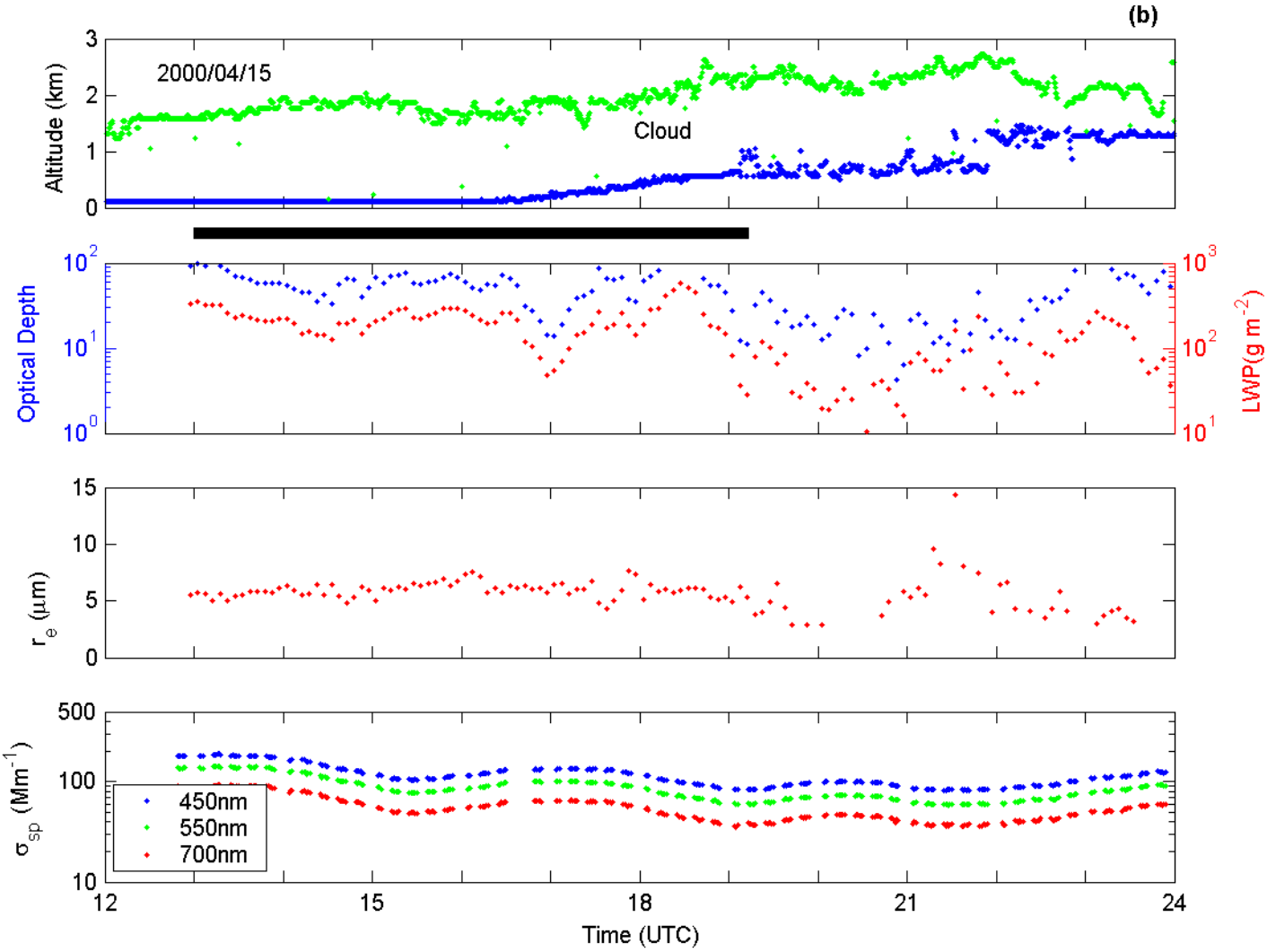
(b)
2000/04/15
Cloud
Altitude (km)
Optical Depth
LWP(g m^{-2})
r_e (μm)
σ_{sp} (Mm^{-1})
450nm
550nm
700nm
Time (UTC)

Figure 3

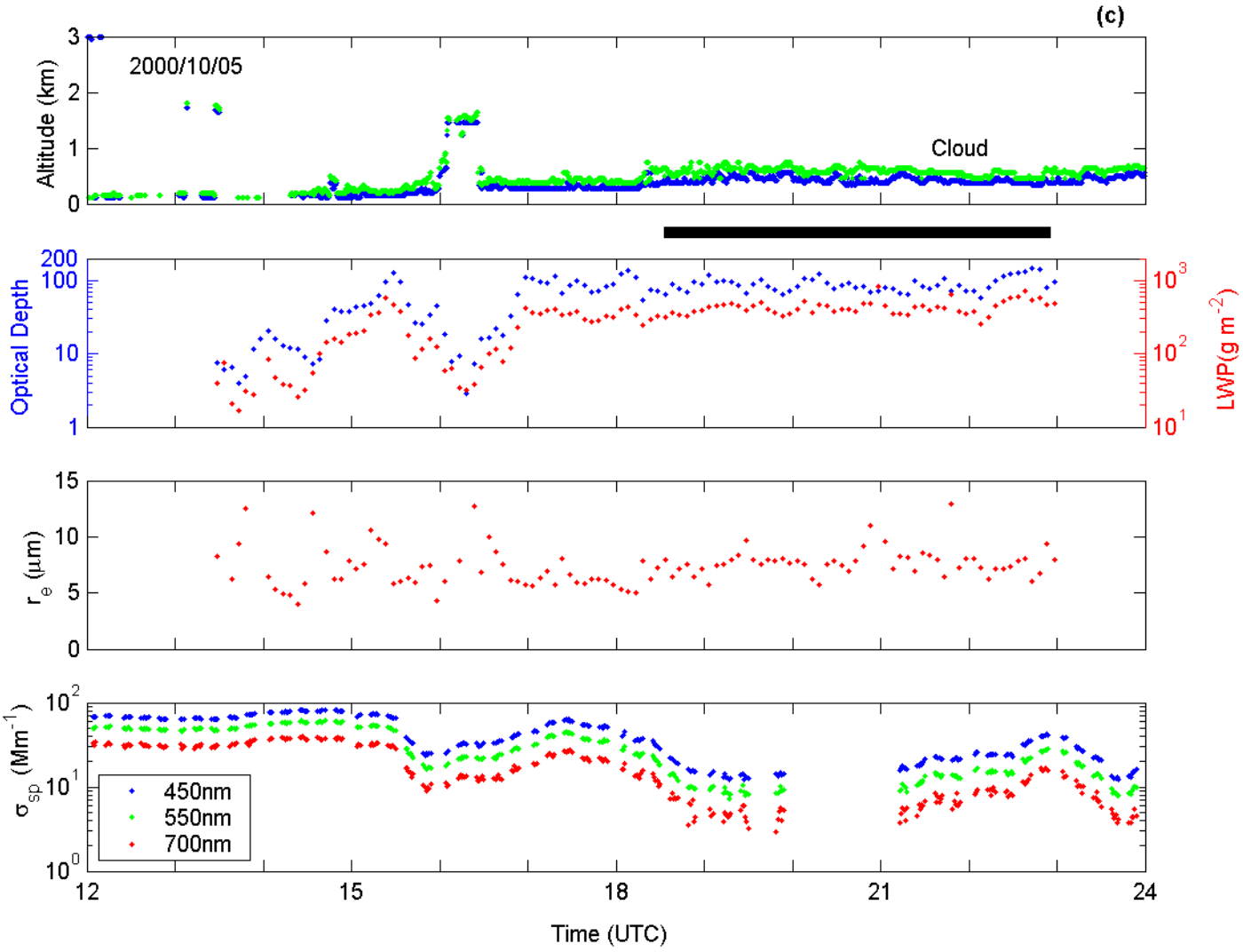
(c)
2000/10/05
Altitude (km)
Cloud
Optical Depth
LWP(g m-2)
re (μm)
σsp (Mm-1)
450nm
550nm
700nm
Time (UTC)

Figure 3

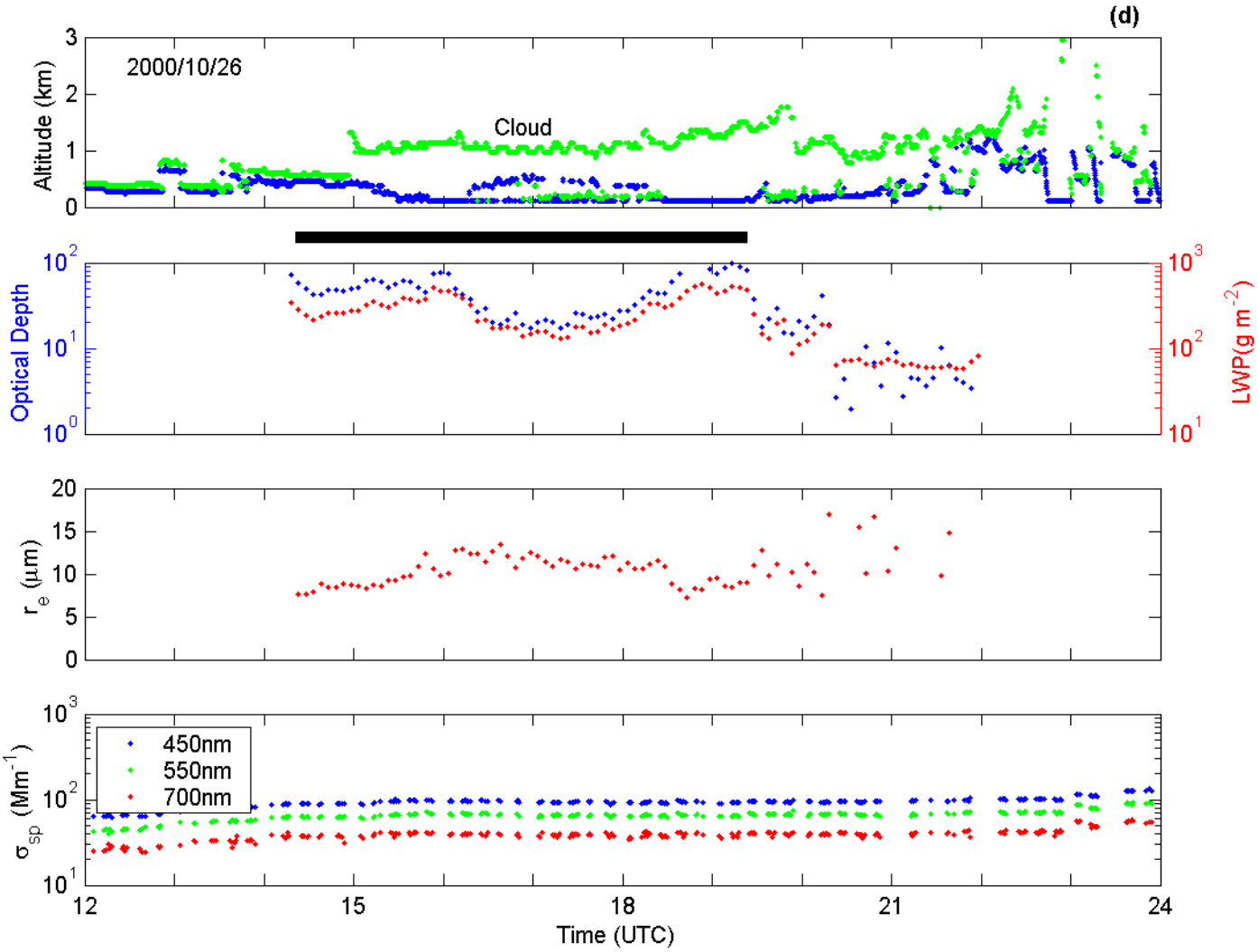
(d)
2000/10/26
Cloud
Altitude (km)
Optical Depth
LWP(g m-2)
re (μm)
σsp (Mm-1)
450nm
550nm
700nm
Time (UTC)

Figure 3

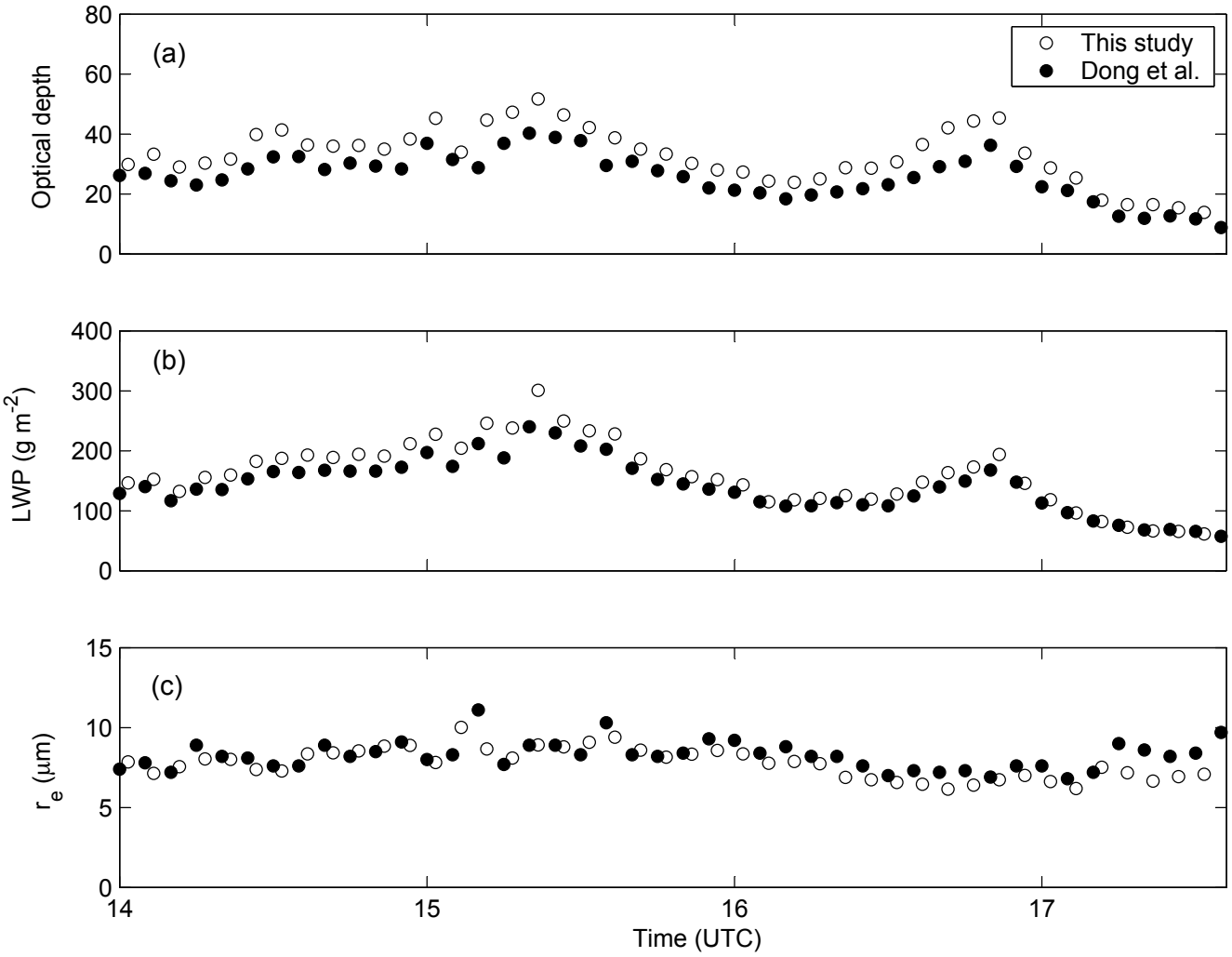
(a)
(b)
(c)
This study
Dong et al.
Optical depth
LWP (g m-2)
re (μm)
Time (UTC)
0
20
40
60
80
100
200
300
400
5
10
15
14
15
16
17

Figure 4

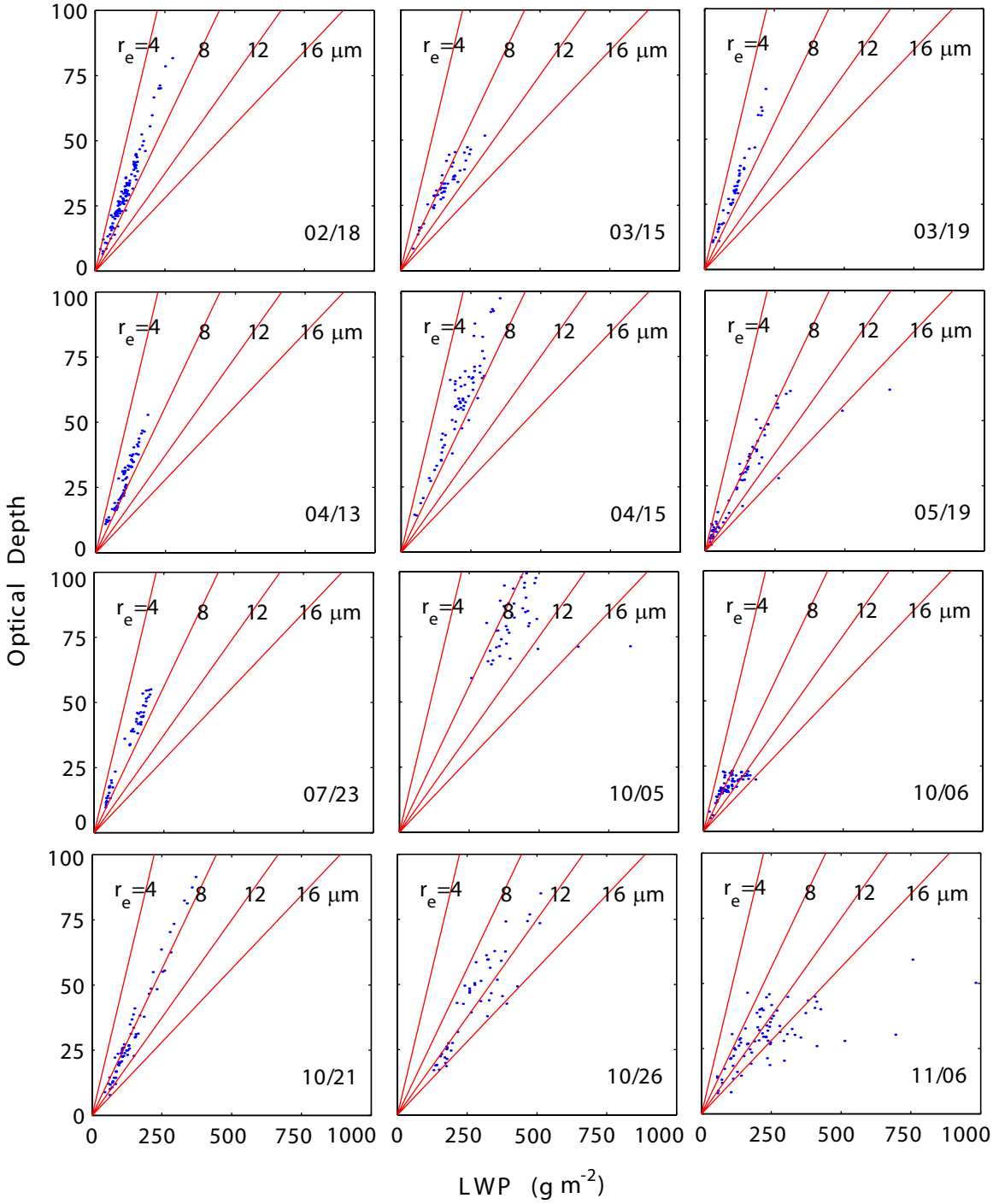
Optical Depth
LWP (g m-2)
re=4 8 12 16 μm
02/18
03/15
03/19
04/13
04/15
05/19
07/23
10/05
10/06
10/21
10/26
11/06
0 25 50 75 100
0 250 500 750 1000

Figure 5

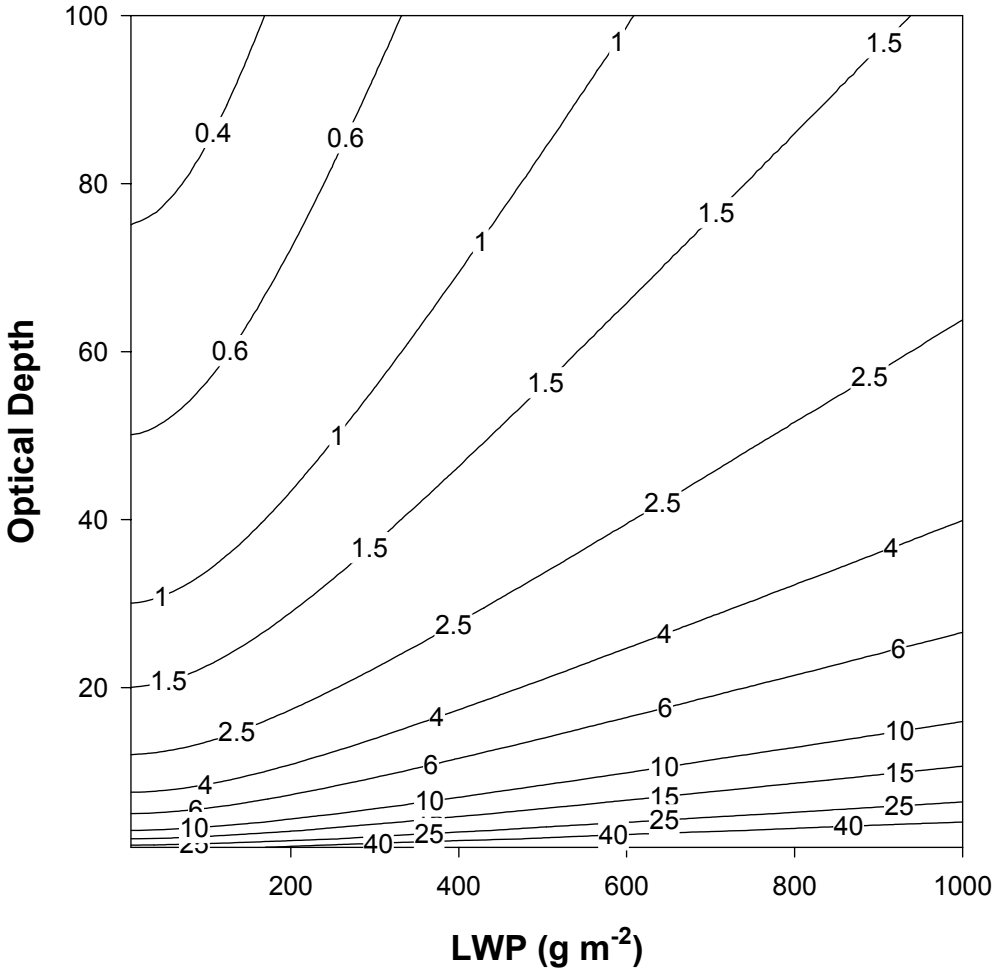
Optical Depth
LWP (g m-2)
100
80
60
40
20
200
400
600
800
1000
0.4
0.6
1
1.5
2.5
4
6
10
15
25
40

Figure 6

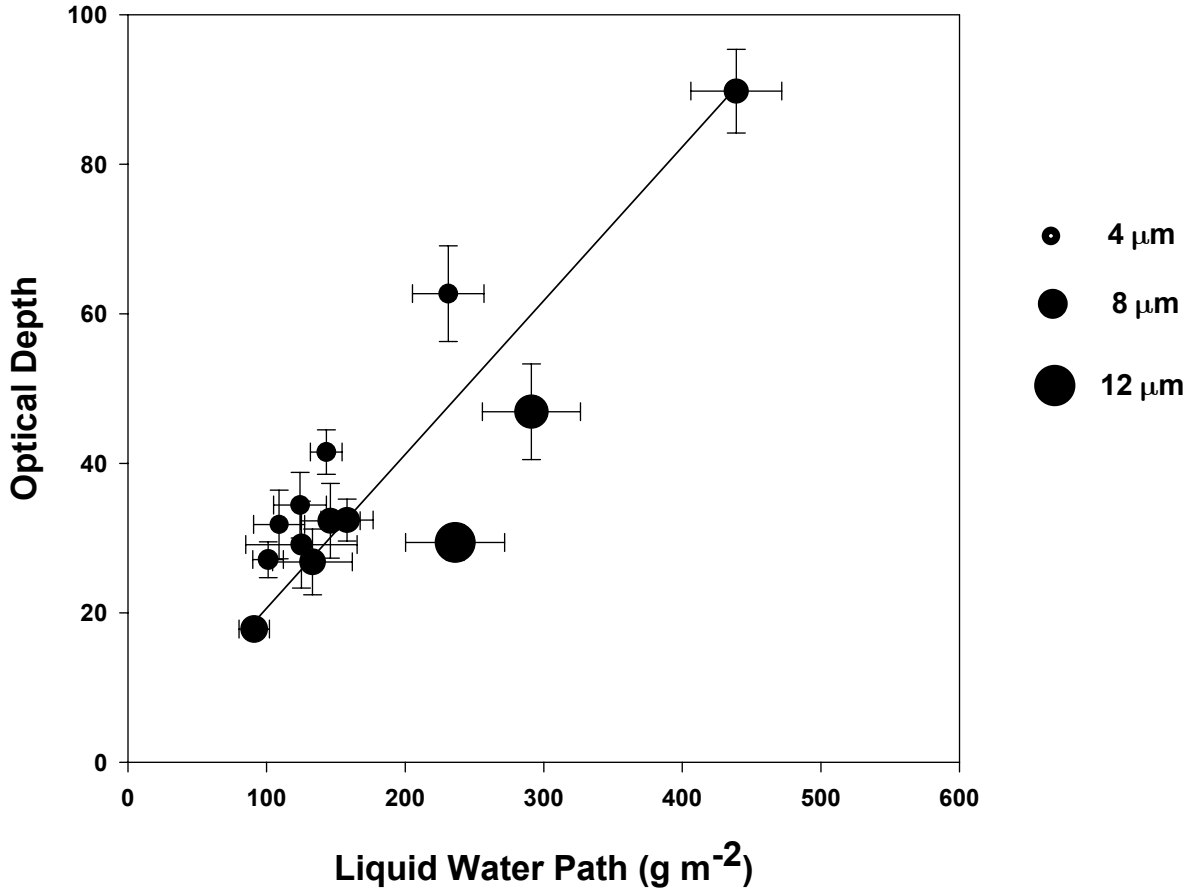
Optical Depth
Liquid Water Path (g m-2)
0
20
40
60
80
100
0
100
200
300
400
500
600
4 μm
8 μm
12 μm

Figure 7

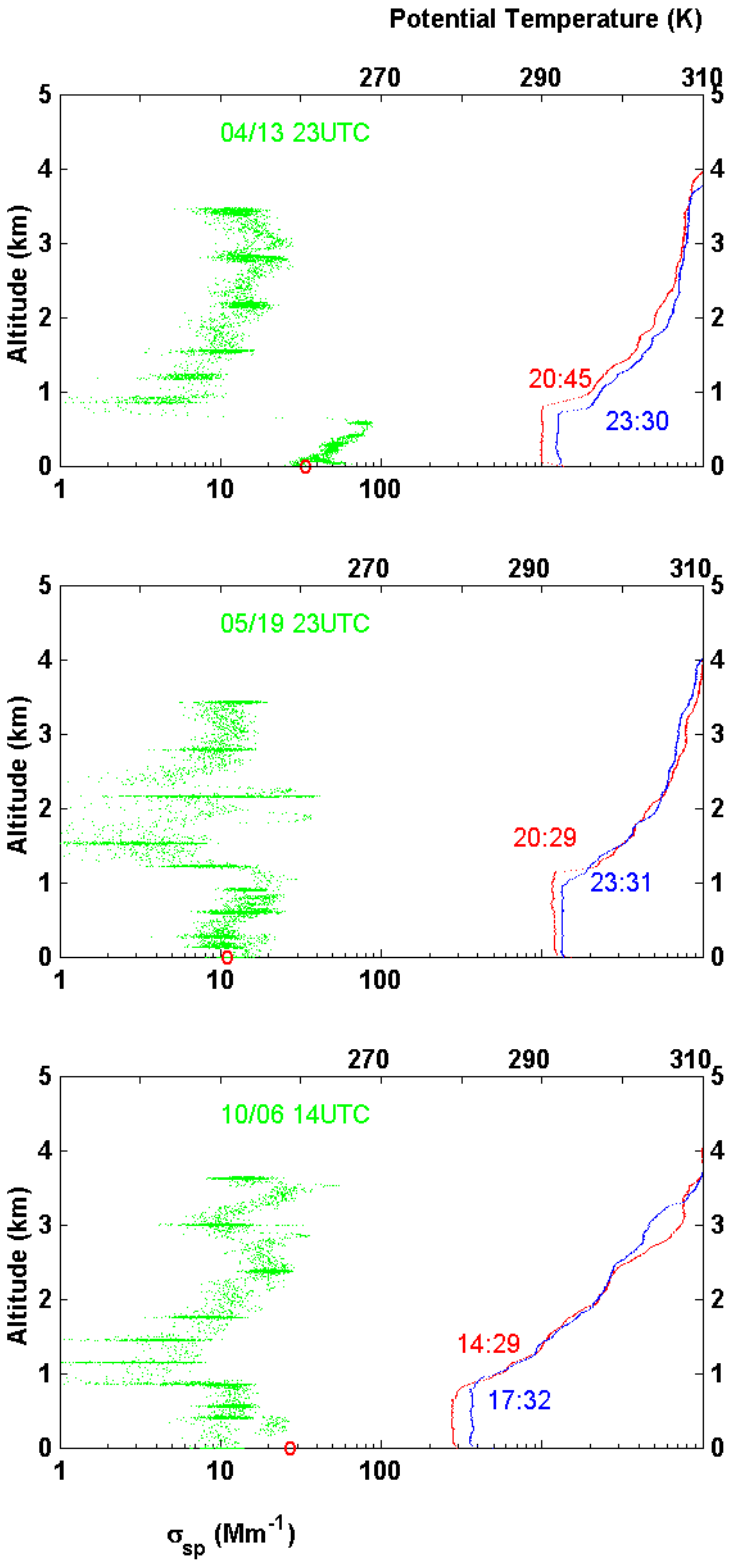
Potential Temperature (K)
270
290
310
04/13 23UTC
20:45
23:30
05/19 23UTC
20:29
23:31
10/06 14UTC
14:29
17:32
Altitude (km)
0
1
2
3
4
5
1
10
100
σsp (Mm-1)

Figure 8

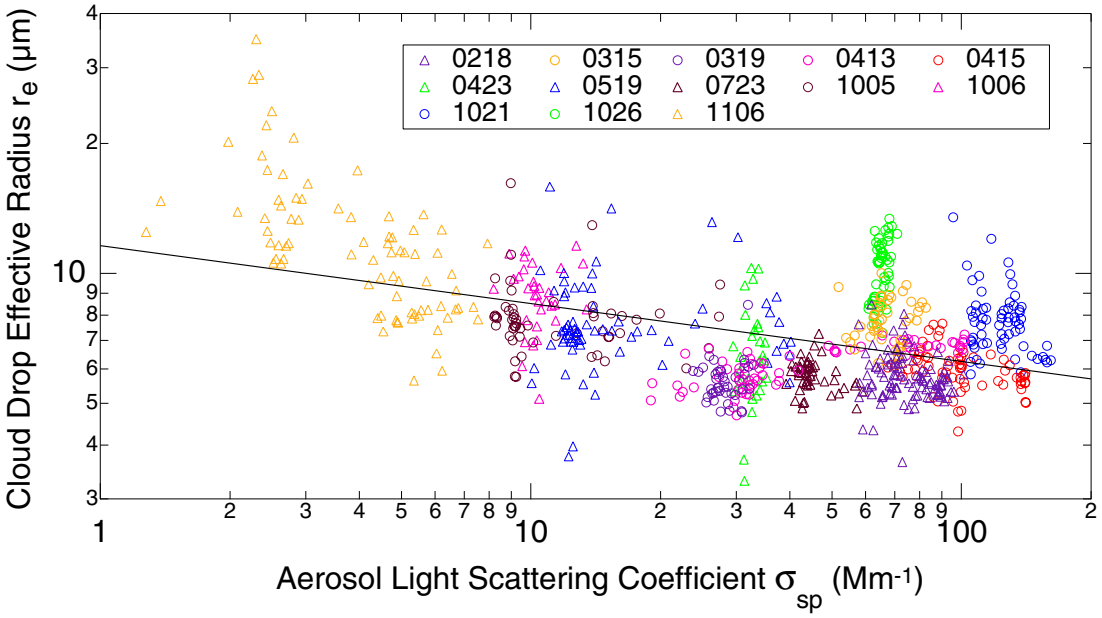
Cloud Drop Effective Radius r_e (μm)
Aerosol Light Scattering Coefficient σ_{sp} (Mm^{-1})
0218
0315
0319
0413
0415
0423
0519
0723
1005
1006
1021
1026
1106

Figure 9

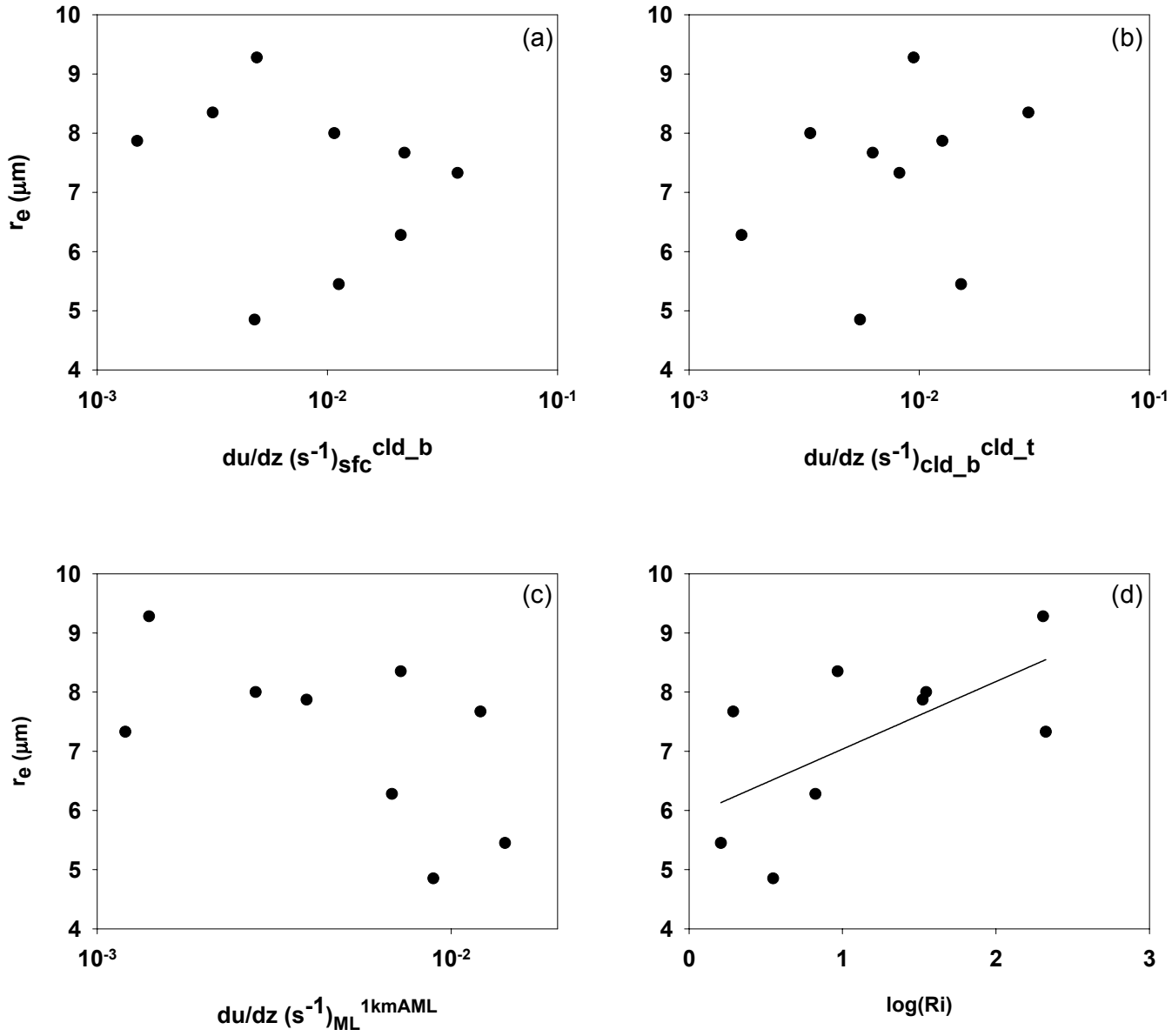
(a)
(b)
(c)
(d)
10
9
8
7
6
5
4
r_e (μm)
10^{-3}
10^{-2}
10^{-1}
$du/dz\ (s^{-1})_{sfc}^{cld\_b}$
$du/dz\ (s^{-1})_{cld\_b}^{cld\_t}$
$du/dz\ (s^{-1})_{ML}^{1kmAML}$
0
1
2
3
log(Ri)

Figure 10

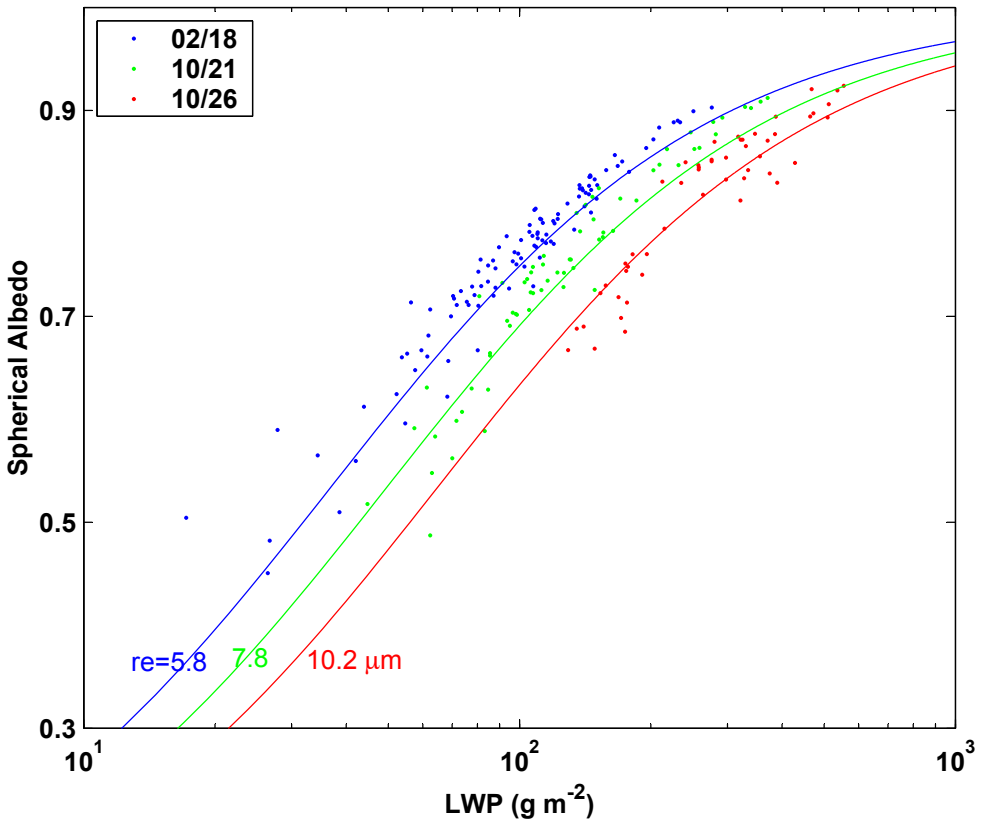
02/18
10/21
10/26
0.9
0.7
0.5
0.3
Spherical Albedo
re=5.8
7.8
10.2 μm
10^1
10^2
10^3
LWP (g m^-2)

Figure 11

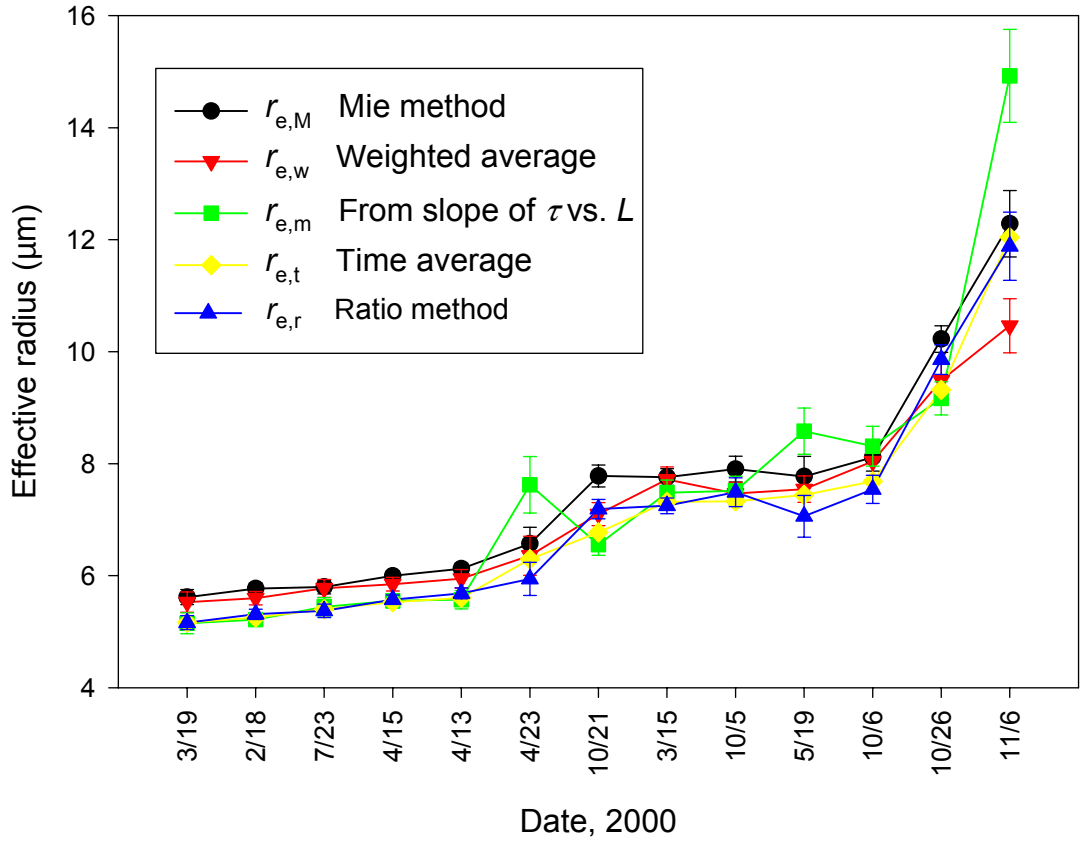
16
14
12
10
8
6
4
Effective radius (μm)
$r_{e,M}$ Mie method
$r_{e,w}$ Weighted average
$r_{e,m}$ From slope of τ vs. L
$r_{e,t}$ Time average
$r_{e,r}$ Ratio method
3/19
2/18
7/23
4/15
4/13
4/23
10/21
3/15
10/5
5/19
10/6
10/26
11/6
Date, 2000

Figure A1